Reduction of the wave propagation error of a sigma grid based numerical tank using a vertical spacing based on the constant truncation error

Csaba Pakozdi*[1], Weizhi Wang[2], Arun Kamath[2], and Hans Bihs[2]

[1]SINTEF Ocean, Otto Nielsens vei 10, 7052 Trondheim, Norway
[2]Department of Civil and Environmental Engineering, Norwegian University of Science and Technology (NTNU), 7491 Trondheim, Norway

Ocean Engineering, 2021, **239** , pp. 109741.
DOI: http://dx.doi.org/10.1016/j.oceaneng.2021.109741

Abstract

Numerical wave models that solve the Laplace equation for the velocity potential with a σ-grid in the vertical direction have been proven to be flexible and efficient. However, it is observed that the dispersion relation is sensitive to the variation of the vertical σ-grid arrangements. So far, there is no recommended practice to optimise the vertical σ-grid for a correct representation of the dispersion relation. In order to reduce the uncertainty of the dispersion relation and optimise the choice of the vertical grid distribution, a new method based on the constant truncation error of the finite difference scheme is presented in this article. The optimised vertical grids estimated by the novel method are applied in the fully nonlinear potential flow model REEF3D::FNPF to provide simulated wave surface elevations, which are compared with the measured time series in the long wave flume at SINTEF Ocean, Trondheim. Several different wave scenarios are considered, including regular waves, bichromatic waves, trichromatic waves as well as irregular waves. The wavemaker motions in the physical flume are used to generate waves in the numerical wave tank of REEF3D::FNPF. The proposed truncation error method is seen to effectively mitigate the dispersion (phase) error in all scenarios and the simulations show high accuracy in comparison with the experimental data.

Keywords: Numerical Wave Tank; Potential Flow Theory; Sigma Grid; Dispersion; Finite Difference Method; REEF3D

*Corresponding author,csaba.pakozdi@sintef.no
Postprint, published in Ocean Engineering, doi:http://dx.doi.org/10.1016/j.oceaneng.2021.109741

1 Introduction

Numerical reproduction of a design sea state is often the first and vital step in the design process of offshore and ocean engineering. Potential flow theory based wave models are often utilised for such numerical simulations due to their high computational efficiency. A few potential flow models have been developed using different techniques to solve for the velocity potential from the Laplace equation and the corresponding boundary conditions.

One of the widely used technique is the boundary element method (BEM) Grilli et al. (1994, 2001). The BEM based models are seen to be computationally efficient for small computational domains. However, it is challenging to implement high-order numerical schemes and parallel computation in a BEM model due to the fully populated unsymmetrical matrix. Li and Fleming Li and Fleming (1997) introduced a three-dimensional (3D) fully nonlinear potential flow model where the Laplace equation and boundary conditions are solved using the finite difference method (FDM) and a multigrid solver. A σ-grid is used in the vertical direction allowing the grid to follow the variations of the free surface as well as the bottom. Based on this method, Bingham and Zhang Bingham and Zhang (2007) and Engsig-Karup et al. Engsig-Karup et al. (2009) introduced higher-order numerical schemes and developed the general purpose flexible-order model OceanWave3D. The potential flow model using a finite difference method and σ-grid proves to be both computationally efficient and flexible regarding irregular bathymetry. It is also straightforward to implement parallel computation using domain-decomposition technique. In a recent development, a Graphics Processing Unit (GPU)-accelerated model is also presented Engsig-Karup et al. (2012); Glimberg et al. (2013). Another method to solve for the velocity potential is the high-order spectral (HOS) method Ducrozet et al. (2012); Bonnefoy et al. (2006a,b); Raoult et al. (2016); Yates and Benoit (2015). With the efficient usage of Fast Fourier Transform (FFT), the HOS models demonstrate high computational speed have been observed, especially over constant bathymetry with and open boundaries. However, the treatments of irregular bathymetry and breaking waves are challenging in comparison to FDM-based models. Considering both computational efficiency and flexibility, the FDM-based models with σ-grid arrangement is seen to be ideal for general applications for a wide range of scenarios. Following this strategy, a fully nonlinear potential flow model REEF3D::FNPF Bihs et al. (2020); Wang et al. (2019) has been developed within the open-source hydrodynamic framework REEF3D Bihs et al. (2016).

The σ-coordinate system is able to capture the exact locations of the time-variant boundaries and ensure that the correct boundary conditions are implemented at the correct locations. The stretching of the vertical grid reduces the computational cost as well as the numerical errors from the same number of grid points. However, the dispersion relation is sensitive to the vertical grid arrangement. The number of the grid points in the vertical direction and the strength of the stretching functions have significant influence on the accuracy of the dispersion relation in the numerical wave tank (NWT).

An empirical understanding of the effects on the dispersion relations from the vertical grid arrangement has been investigated by Engsig-Karup et al. Engsig-Karup et al. (2009) through a convergence study of the different vertical grid arrangements. Based on this study, the number of the vertical grid points required to achieve a grid independent solution is very high: from tens to several hundreds of grid points depending on the order of the applied scheme. The large number of grid points demands large computational resources and long computational time which would significantly limit the practical application area of a numerical wave tank.

However, in a similar study Bingham and Zhang (2007), it was observed that the stretching factor for the vertical stretching function also has significant influence on the representation of the dispersion relation. Sometimes, a simulation with a lower number of vertical grid points yields better results than the one with a larger number of vertical grid points due to different choices of the stretching factor. Thus, it is important to optimise the choice of the stretching factor in addition to the refinement of the vertical grid in order to reach a grid independent solution and represent the dispersion relation accurately. The balance and optimisation between the two factors, the number of vertical grid points and the stretching factor, provide a pragmatic and efficient way to mitigate the phase errors while remaining high computational speed.

To the authors knowledge, there is no recommended procedure to estimate and calculate the optimal vertical stretching to date. Therefore, a novel optimisation scheme of the vertical grid arrangement is introduced in the presented work to minimise the errors in dispersion relation and maximise the advantage of the σ-coordinate system and the vertical grid stretching. The concept behind the new method is that the wave propagation error is linked to the truncation error of the applied numerical scheme in the vertical direction and this error depends on the distances between the vertical grid points. The truncation error is large for grids with few vertical grid point. By keeping a constant truncation error in the vertical direction, not the size of the error, but the influence of this error on the distribution can be mimimize and a correct phase velocity can be achieved. This condition, the constant truncation error in the vertical direction is used to define the locations of the vertical grid points.

The fully nonlinear potential flow model REEF3D::FNPF is used in the study to confirm the effectiveness of the novel method. REEF3D::FNPF solves the Laplace equation using a finite difference method on a σ-coordinate grid. The model inherits the high-order spatial and temporal discretisation schemes and parallel computation using domain decomposition from the open-source hydrodynamic framework REEF3D Bihs et al. (2016). The framework has shown high accuracy and stability through a wide range of applications with different solvers, such as breaking wave force Alagan Chella et al. (2019), complex structure response Aggarwal et al. (2020); Sasikumar et al. (2020), floating structures Martin et al. (2020) and sediment transport Ahmad et al. (2020). With the open-source nature and numerical robustness, the potential flow module REEF3D::FNPF provides an ideal platform to test the novel method. In the REEF3D::FNPF numerical wave tank, the wavemaker motions from the long wave flume at SINTEF Ocean Onorato et al. (2004) are used to generate four different types of wave fields and the simulated results using the novel optimisation method are compared to the measured time series in the same wave flume.

The article is organised as the following. First, the numerical schemes of the model REEF3D::FNPF as well as its vertical grid stretching algorithm are introduced in section 2. Then, the novel method to optimise the vertical stretching of the σ-grid based on constant truncation error is described in detail in section 3. In order to confirm the effectiveness of the method, a verification is performed using a regular wave simulation in the NWT of REEF3D::FNPF as shown in section 4. Thereafter, the novel method is used for the simulations of a wide range of wave scenarios and the simulation results are validated in section 5. In the end, the observations during the verification and validations are summarised and conclusions are drawn in section 6.

2 Numerical Model

As mentioned in the introduction, the fully nonlinear potential flow model REEF3D::FNPF is used to test the proposed novel optimisation method. The governing equation for the model is the Laplace equation:

$$\frac{\partial^2 \Phi}{\partial x^2} + \frac{\partial^2 \Phi}{\partial y^2} + \frac{\partial^2 \Phi}{\partial z^2} = 0. \tag{1}$$

Boundary conditions are required in order to solve for the velocity potential Φ from this elliptic equation, especially at the free surface and at the bed. These are the kinematic and dynamic boundary conditions which must be fulfilled at all times and are prescribed as follows:

$$\frac{\partial \eta}{\partial t} = -\frac{\partial \eta}{\partial x}\frac{\partial \widetilde{\Phi}}{\partial x} - \frac{\partial \eta}{\partial y}\frac{\partial \widetilde{\Phi}}{\partial y} + \widetilde{w}\left(1 + \left(\frac{\partial \eta}{\partial x}\right)^2 + \left(\frac{\partial \eta}{\partial y}\right)^2\right), \tag{2}$$

$$\frac{\partial \widetilde{\Phi}}{\partial t} = -\frac{1}{2}\left(\left(\frac{\partial \widetilde{\Phi}}{\partial x}\right)^2 + \left(\frac{\partial \widetilde{\Phi}}{\partial y}\right)^2 - \widetilde{w}^2\left(1 + \left(\frac{\partial \eta}{\partial x}\right)^2 + \left(\frac{\partial \eta}{\partial y}\right)^2\right)\right) - g\eta \tag{3}$$

where η is the free surface elevation, $\widetilde{\Phi} = \Phi(\mathbf{x}, \eta, t)$ is the velocity potential at the free surface, $\mathbf{x} = (x, y)$ represents the location at the horizontal plane and $\widetilde{w}$ is the vertical velocity at the free surface.

The bottom boundary condition represents an impervious solid boundary:

$$\frac{\partial \Phi}{\partial z} + \frac{\partial h}{\partial x}\frac{\partial \Phi}{\partial x} + \frac{\partial h}{\partial y}\frac{\partial \Phi}{\partial y} = 0, \quad z = -h. \tag{4}$$

where $h = h(\mathbf{x})$ is the water depth measured from the still water level to the seabed.

The Laplace equation with the boundary conditions is solved with a finite difference method on a σ-coordinate system. A σ-coordinate system deforms with the free surface and is also flexible in the handling of irregular boundaries. The relationship between a Cartesian grid and a σ-coordinate is as follows:

$$\sigma = \frac{z + h\left(\mathbf{x}\right)}{\eta(\mathbf{x}, t) + h(\mathbf{x})}. \tag{5}$$

Several methods are implemented in REEF3D for grid stretching in horizontal and vertical direction. One of them uses the sinh function as the stretching function:

$$\tilde{\sigma} = 1 - \frac{\sinh\left(\delta\sigma\right)}{\sinh\left(\delta\right)} \tag{6}$$

where σ is the uniform σ-coordinates, δ is the above mentioned stretching factor and $\tilde{\sigma}$ is the new σ-coordinates. $\tilde{\sigma}$ will be referred as σ further in this paper. This stretching method gives the closest grid location to the optimal grid positions with the proper choice of σ and the number of the vertical grid points. This stretching method is used in the simulations.

Once the velocity potential Φ is obtained in the σ-domain, the velocities can be calculated as follows:

$$u\left(\mathbf{x},z\right)=\frac{\partial\Phi\left(\mathbf{x},z\right)}{\partial x}=\frac{\partial\Phi\left(\mathbf{x},\sigma\right)}{\partial x}+\frac{\partial\sigma}{\partial x}\frac{\partial\Phi\left(\mathbf{x},\sigma\right)}{\partial\sigma}, \tag{7}$$

$$v\left(\mathbf{x},z\right)=\frac{\partial\Phi\left(\mathbf{x},z\right)}{\partial y}=\frac{\partial\Phi\left(\mathbf{x},\sigma\right)}{\partial y}+\frac{\partial\sigma}{\partial y}\frac{\partial\Phi\left(\mathbf{x},\sigma\right)}{\partial\sigma}, \tag{8}$$

$$w\left(\mathbf{x},z\right)=\frac{\partial\Phi\left(\mathbf{x},z\right)}{\partial z}=\frac{\partial\sigma}{\partial z}\frac{\partial\Phi\left(\mathbf{x},\sigma\right)}{\partial\sigma}. \tag{9}$$

Wave generation in the numerical wave tank is handled using a Neumann boundary condition. Here, the spatial derivatives of the velocity potential are prescribed according to the wavemaker kinematics. The velocity potential at the boundary can then be calculated as follows:

$$\varphi_{i-1}=-u(\boldsymbol{x},z,t)\triangle x+\varphi_i \tag{10}$$

where $u(\boldsymbol{x},z,t)$ is the analytical horizontal velocity. The wavemaker motion is defined through a file where a time series of the angle of the flaps are defined. The measured flap angles are used in this paper to generate the waves.

The numerical beach uses the relaxation method Mayer et al. (1998) to mitigate wave reflection. The relaxation function used in the model is shown in Eqn. (11).

$$\Gamma(\widetilde{x})=1-\frac{e^{(\widetilde{x}^{3.5})}-1}{e-1}\ for\ \widetilde{x}\in[0;1]. \tag{11}$$

where $\widetilde{x}$ is scaled to the length of the relaxation zone.

The Laplace equation is discretised using a second-order central difference scheme and is solved using a parallelised geometric multi-grid pre-conditioned conjugated gradient solver provided by Hypre Falgout et al. (2006).

The convection terms at the free-surface are discretised with the fifth-order Hamilton–Jacobi weighted essentially non-oscillatory (WENO) scheme Guang-Shan and Chi-Wang (1996). A WENO discretisation stencil is based on smoothness of three local ENO-stencils. The local stencil with the highest smoothness is assigned the highest weight and contributes the most significantly to the solution. The scheme is therefore capable of handling large gradients without instability.

For the time treatment, a third-order accurate TVD Runge-Kutta scheme Chi-Wang and Stanley (1988) is used with constant time step.

The model is fully parallelised following the domain decomposition strategy. Ghost cells are used to exchange information between adjacent domains and are updated with the values from the neighbouring processors using the Message Passing Interface (MPI).

3 Estimation of The Optimal Vertical Grid Distribution

3.1 Description of the methodology

The truncation error of a finite difference scheme with a given order can be typified from a Taylor series of a function $f(z)$ at the location ζ with a finite number of components,

which equals with the order of the scheme. As an example, the Taylor expansion up to the fourth-order accuracy shown here:

$$\begin{aligned} f(z) =& f(\zeta) + \frac{df(\zeta)}{dz}(z-\zeta) + \frac{1}{2}\frac{d^2f(\zeta)}{dz^2}(z-\zeta)^2 + \frac{(1}{6}\frac{d^3f(\zeta)}{dz^3}(z-\zeta)^3 \\ &+ \frac{1}{24}\frac{d^4f(\zeta)}{dz^4}(z-\zeta)^4 + O((z-\zeta)^5)\,. \end{aligned} \tag{12}$$

The value of the truncation error in Eqn. (12), $O((z-\zeta)^5)$ depends on $(z-\zeta)$, the distance between the grid points and the location ζ where the Taylor series is expanded. It shows that the absolute value of the truncation error varies along a uniformly distributed grid. Therefore it is beneficial to use a non-uniform grid to reduce the truncation error without increasing the number of the grid points.

The proposed novel method uses the solution of the Airy wave theory. The solution of the Airy wave theory for regular wave is based on the separation of variables method (Dean and Dalrymple, 1991):

$$\phi(x,z,t) = \Phi(z)\Xi(x)\Upsilon(t). \tag{13}$$

The vertical distribution of the velocity potential $\Phi(z)$ is written as the following:

$$\Phi(z) = C\mathrm{e}^{kz} \quad \text{for infinite water depth} \tag{14}$$

$$\Phi(z) = C\frac{\cosh\left(k\left(z+h\right)\right)}{\cosh\left(kh\right)} \quad \text{for finite water depth} \tag{15}$$

It is observed that the distribution is governed only by the wave number k, which is defined by the linear dispersion relationship between the angular wave frequency ω and the wave number:

$$\omega^2 = gk \quad \text{for infinite water depth} \tag{16}$$

$$\omega^2 = gk\tanh\left(kh\right) \quad \text{for finite water depth} \tag{17}$$

where g is the gravity acceleration and h is the water depth.

It is assumed that the numerically estimated profile of the velocity potential along a vertical line defines a different shape than prescribed by theory due to numerical error. This discrepancy results in an incorrect wave number in the numerical simulation. Consequently, the wave propagation velocity c_{ph} is also incorrect since it depends on the wave number and the wave frequency:

$$c_{ph} = \omega/k\,. \tag{18}$$

The errors resulting from the incorrect representation of the shape of the vertical velocity potential profile is considered to be directly related to the truncation error of the applied numerical scheme. The new method is based on the assumption that a constant absolute truncation error at every vertical location can preserve the correct shape of the function $\Phi(z)$ and yield the correct wave number.

This criterion can be formulated into an equation for the unknown $\Delta z(\zeta) = (z-\zeta)$ from the definition of the Taylor series:

$$f(z) = \sum_{n=0}^{\infty}\frac{f(\zeta)^{(n)}}{n!}\left(z-\zeta\right)^n = \sum_{n=0}^{\infty}\frac{f(\zeta)^{(n)}}{n!}\Delta z(\zeta)^n \tag{19}$$

where $f(\zeta)^{(n)}$ is the n-th derivative of ($f(z)$ with respect to z at the location $z = \zeta$. An O-th order scheme is accurate up to $n = O$ i.e., the truncation error at the location ζ can be represented as:

$$\begin{aligned} E(z,\zeta) =& f(z) - \sum_{n=0}^{O} \frac{f(\zeta)^{(n)}}{n!}\Delta z(\zeta)^n = \sum_{n=0}^{\infty} \frac{f(\zeta)^{(n)}}{n!}\Delta z(\zeta)^n - \sum_{n=0}^{O} \frac{f(\zeta)^{(n)}}{n!}\Delta z(\zeta)^n \\ =& \sum_{n=O+1}^{\infty} \frac{f(\zeta)^{(n)}}{n!}\Delta z(\zeta)^n \end{aligned} \tag{20}$$

If the size of the absolute error is set to a constant E for every vertical location ζ and the function $f(z)$ and its derivatives are known, one can find the correct step Δz for every location ζ:

$$E = \sum_{n=O+1}^{\infty} \frac{f(\zeta)^{(n)}}{n!}\Delta z(\zeta)^n \tag{21}$$

3.2 Vertical grid optimisation based on the Airy wave theory for infinite water depth

According to the Airy wave theory for infinite water depth, the function of the solution which only depends on the variable z is defined as (Dean and Dalrymple, 1991):

$$\Phi(z) = \frac{\zeta_A g}{\omega} \mathrm{e}^{kz} \tag{22}$$

where ζ_A is the wave amplitude. We can normalise this function with $\dfrac{\zeta_A g}{\omega}$, which gives a more general result for the analysis. The nth derivative of this normalised function with respect to z is:

$$\Phi(z)^{(n)} = k^n \mathrm{e}^{kz} \tag{23}$$

From here, the Taylor series at $z = \zeta + \Delta z$ is expressed as:

$$\mathrm{e}^{k(\zeta+\Delta z)} = \mathrm{e}^{k\zeta} \sum_{n=0}^{\infty} \frac{(k\Delta z)^n}{n!}\,. \tag{24}$$

Using the condition defined in Eqn. (21) one can define a grid size at each ζ by solving:

$$0 = E\mathrm{e}^{-k\zeta} - \sum_{n=O+1}^{\infty} \frac{(k\Delta z)^n}{n!} \tag{25}$$

for a scheme of order O. It is possible to generalise this equation for all wave numbers by introducing two dimensionless variables: $kz = k \cdot \zeta$ and $kdz = k \cdot \Delta z$:

$$0 = E\mathrm{e}^{-kz} - \sum_{n=O+1}^{\infty} \frac{kdz^n}{n!} \tag{26}$$

This equation has no analytical solution and must be solved numerically. The MATLAB `fzero` function is used to solve the problem iteratively. It is necessary to define an initial

value of the size of kdz at each kz location in order to obtain a numerical solution. Eqn. (26) can be rewritten when only the first summand is used:

$$0 = E\mathrm{e}^{-kz} - \sum_{n=O+1}^{O+1} \frac{kdz^n}{n!} = E\mathrm{e}^{-kz} - \frac{kdz^{(O+1)}}{(O+1)!} \tag{27}$$

Thereafter, kdz can be directly calculated as:

$$kdz = \sqrt[(O+1)]{E\mathrm{e}^{-kz}\left[(O+1)!\right]}\,. \tag{28}$$

An initial value is estimated at the beginning of each iteration. It becomes apparent that the calculation of the summation in Eqn. (26) up to $O + 20$ is sufficient.

Only the results for the second- and fourth-order schemes are presented in this paper. The

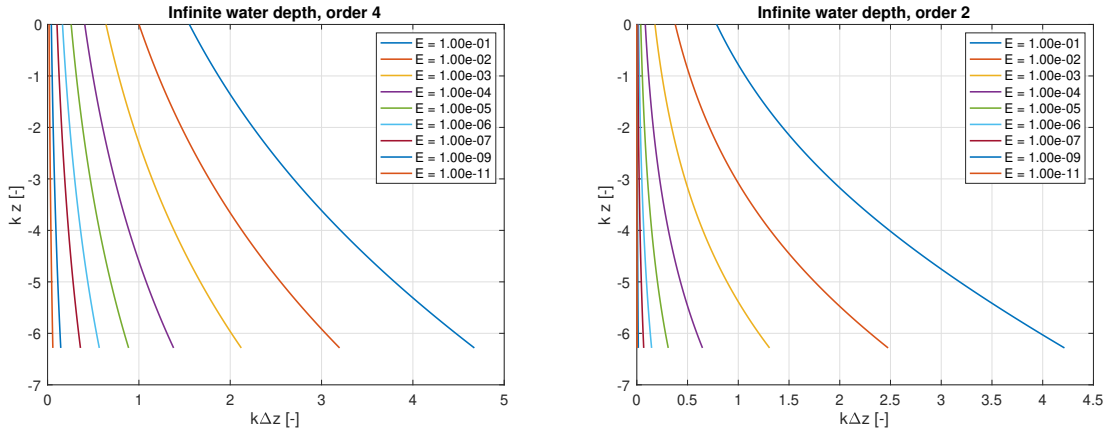

(a) Fourth order scheme

(b) Second order scheme

Figure 1: Grid size for different error levels E for infinite water depth.

solution for different E is presented in Figure 1a for the fourth order scheme ($O = 4$). The x-axis defines the normalised grid height at the normalised z location shown on the y-axis of the diagram. A smaller constant error E yields a smaller grid height. The grid size increases with water depth as Φ decreases exponentially with increasing depth. The solutions are shown up to $kz = 2\pi$ below the still water level as it is assumed that $\Phi(z < -2\pi/k)$ is constant below one wavelength from the mean water level $z = 0$ and that the same grid size can be used below this depth. It is seen that the grid height decreases at a near quadratic rate for the fourth order scheme. Similarly, the solution for different E for the second order scheme ($O = 2$) is shown in Figure 1b.

3.3 Vertical grid optimisation based on the Airy wave theory for finite water depth

For finite water depth, the function of the vertical velocity potential profile depends on the variable z as well as the water depth h. The normalised function according to the Airy wave

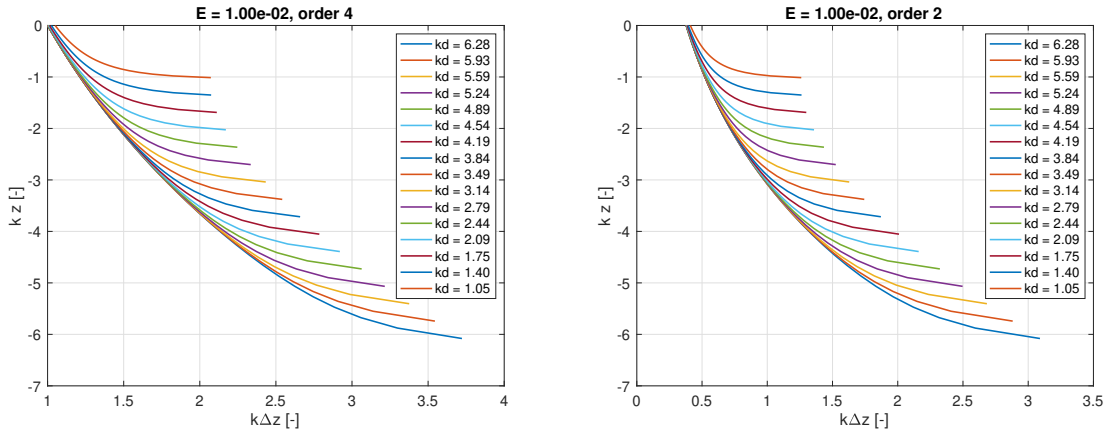

(a) Fourth order scheme

(b) Second order scheme

Figure 2: Grid size for different normalised water depth and for error level $E = 0.02$, finite water depth.

theory is defined as (Dean and Dalrymple, 1991):

$$\Phi(z,d) = \frac{\cosh\left(k\left(z+h\right)\right)}{\cosh\left(kh\right)} = \frac{\left(e^{2k(z+h)}+1\right)e^{-kz}}{e^{2kh}+1}\,. \tag{29}$$

In order to define its Taylor expansion at ζ it is favourable to formulate its n-th derivative in a similar way as in Eqn. (23):

$$\Phi^{(n)}(z) = k^n \frac{\left(e^{2k(z+h)}+(-1)^n\right)e^{-kz}}{e^{2kh}+1} \tag{30}$$

where Eqn. (23) is used to develop this formulation. This yields its Taylor expansion at $z = \zeta + \Delta z$ following Eqn. (19):

$$\Phi(z) = \sum_{n=0}^{\infty} \frac{(k\Delta z)^n}{n!} \frac{\left(e^{2k(\zeta+h)}+(-1)^n\right)e^{-k\zeta}}{e^{2kh}+1} = \frac{e^{-k\zeta}}{e^{2kh}+1} \sum_{n=0}^{\infty} \frac{(k\Delta z)^n}{n!} \left(e^{2k(\zeta+h)}+(-1)^n\right)\,. \tag{31}$$

Following the same way as it was shown in the previous paragraph one can define the grid size kdz at each kz for any dimensionless water depth $kh = k \cdot h$ by solving:

$$0 = E - \frac{e^{-kz}}{e^{2kh}+1} \sum_{n=(O)+1}^{\infty} \frac{(kdz)^n}{n!} \left(e^{2kz+2kh}+(-1)^n\right)\,. \tag{32}$$

There does not exist an analytical solution for this equation. It must be solved numerically in the same way as for the infinite water depth case. An initial guess for the size of kdz is estimated from the infinite water depth formula Eqn. (28) to initialise the iterative process.

The solution for different normalised water depths kd for $E = 0.02$ is presented in Figure 2a for the fourth order scheme ($O = 4$). The x-axis defines the normalised grid height at the normalised z-location shown on the y-axis of the diagram. The curves at different water depth

are close to each other near the still water level but change significantly close to the bottom. The grid sizes $k\Delta z$ are significantly larger in comparison to the calculations at infinite water depth.

The solutions for different normalised water depths kd for the second order scheme ($O = 2$) with a constant error of $E = 0.02$ are shown in Figure 2b. It is observed that the cell height does not decrease at a quadratic rate as for the fourth-order scheme.

3.4 Iterative procedure to estimate the vertical spacing for a given wave period

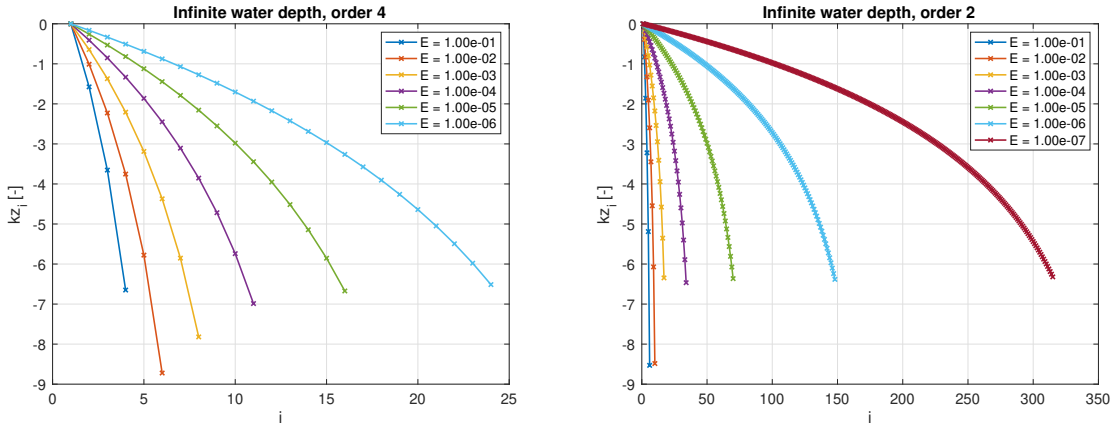

(a) Fourth order scheme

(b) Second order scheme

Figure 3: Locations of the vertical grid points for the second and fourth order schemes for different error levels E for infinite water depth

The ideal vertical spacing curves as a function of the normalised distance from the mean water level (MWL) at $z = 0$ are shown in Figure 1. Using these solutions one can define the vertical grid spacing at $z_1 = 0$. This value defines the location of the next grid point z_2 as $z_1 - k\Delta z(kz = 0)$. The location of the next grid point z_3 can be estimated from the vertical grid spacing value at z_2 from Figure 1 as $z_3 = z_2 - k\Delta z(kz = z_2)$. This way the vertical spacing can be estimated along the water depth generally for all waves:

$$kz_{i+1} = kz_i - k\Delta z(kz = z_i)\,,\; i = 1 \ldots N_z. \tag{33}$$

The normalised vertical locations of the grid for different truncation errors are shown in Figure 3. The horizontal axis shows the index of the grid locations and the vertical axis the normalised location. The use of the high-order scheme significantly reduces the number of the necessary vertical grid points for the same level of truncation error due to the larger grid spacing at the low error levels.

4 Proof of method

A 2nd-order Stokes regular wave is simulated in a NWT with a single flap wave maker over a constant water depth of 5 m to perform a sensitivity study of the following numerical

parameters:

- uniform horizontal resolution $NX = \lambda/dx$: The number of the horizontal grid points per wave length λ where dx is the horizontal grid size
- vertical resolution NZ: The number of the vertical grid points per wave length
- Courant-Friedrichs-Lewy number CFL: The time step dt is calculated using the CFL number, the wave phase velocity c_{ph} and dx: $dt = CFLdx/c_{ph}$
- vertical grid stretching factor δ: The variation of the stretching factor is used to estimate the optimum grid arrangement following the proposed method.

Thirteen simulations are performed in total. The simulation setup is presented in a separate subsection 4.3. The results of the simulations are compared with each other as well as the analytical solution of the linear wave maker theory (Kusumawinahyu et al., 2006).

4.1 Measurement of the similarity of the time series

Time series are compared with each other in terms of the magnitude of the signals and with their correlation to each other. In order to measure the magnitudes of the signal, several methods are used in this paper.

One of them is the Fourier analysis where the amplitudes are estimated for a given time window with the approximation of the Fourier Series by the Discrete-Fourier-Transformation (DFT) of the time series. We used MATLAB `fft` function to apply DFT. In order to reduce the spectral leakage, the length of the time window is chosen to be an integral number of the wave periods for a regular wave and the start and the end of the time windows is chosen at two zero-up-crossing locations.

However, this method does not show the change of the magnitude of the signal over time. Therefore, the Hilbert envelope of the full time series is calculated and compared. The Hilbert envelope is estimated from the Hilbert transform of the time series. The Hilbert transform is computed from the inverse of its Fourier Transform which can be calculated from the Fourier Transform of the time series:

$$\tilde{H}(\omega) = -iF(\omega) \quad \text{for} \quad \omega > 0\,. \tag{34}$$

The envelope is calculated from the magnitude of its inverse Fourier Transform:

$$|H(t)| = \left| \frac{1}{2} \int_{-\infty}^{\infty} \tilde{H}(\omega) \mathrm{e}^{i\omega t} d\omega \right| \tag{35}$$

The Hilbert envelope includes only minimal phase information and cannot be used to quantify the phase differences between two time series.

In order to show how the time series are in phase with each other, the cosine similarity is calculated Bunnik and de Ridder (2018) within a convolution window over the whole time series. The cosine similarity is defined for two vector of attributes, A and B, as:

$$\text{Correlation} = \frac{\sum_{i=1}^{n} A_i B_i}{\sqrt{\sum_{i=1}^{n} A_i^2} \sqrt{\sum_{i=1}^{n} B_i^2}} \tag{36}$$

where A_i and B_i are the components of vectors , A and B are the two time series respectively. The resulting correlation ranges from -1 (anti-phase), to 1 (exactly in phase), with 0 indicating orthogonality or de-correlation, while in-between values indicate intermediate similarity or dissimilarity. This way the correlation between the time series can be displayed over the time axis.

4.2 Estimation of the wave number from the numerical simulations

Several methods are applied to identify the wave number from the numerical simulations. The Fourier analysis in space is used to estimate the wave number and the amplitude based on the location of the free surface at a given time. This method can use only a limited number of point to estimate the wave number. Further, this method does not show the vertical change of the velocity field which is governed by the wave number.

The magnitude of the velocity is independent of the phase:

$$|v| = \sqrt{u^2 + w^2} = \sqrt{A^2\omega^2 \mathrm{e}^{-2kz}\left(\cos^2(\omega t - kx) + \sin^2(\omega t - kx)\right)} = A\omega \mathrm{e}^{-kz}\,. \tag{37}$$

Therefore it is possible to identify the amplitude A, the wave frequency ω and the wave number k with the help of the least square method (LS). The least square problem is defined for these three unknown parameters as:

$$\min_{A,\omega,k} \| A\omega \mathrm{e}^{kz_n} - |v_n| \|_2 \tag{38}$$

where z_n and $|v_n|$ are taken from the result of the simulation of one time point.

The horizontal range of the window is chosen over a stable region far enough from the wave maker and from the numerical beach. The vertical range of the window is limited to the wave length.

Due to small temporal variation of the estimated parameters, an average value of the above mentioned parameters is derived from eighty time steps in this paper (Figure 4).

4.3 Simulation setup

The numerical domain length is set to $L = 60$m, the length of the numerical beach is $L_B = 20$m. As mentioned earlier, the water depth is $h = 5$m. The vertical location of the hinge of the wave maker d is one meter below the mean water level (MWL) . The simulation is 2D with one layer of cells in the y-direction. The definition of these parameters as well as the location and the directions of the applied coordinate system is presented in Figure 5. The free surface elevation is analysed at three locations 10, 15 and 20m from the wave maker.

An overview over all sensitivity simulations is shown in Table 1. Simulation nr. 00 is compared against all other simulations. Four different studies are applied in order to record the effect of these four parameters on the results.

4.4 Results

The vertical locations of the vertical grid points with different stretching factor is shown in Figure 6. The curve with the stretching factor $\delta = 3.5$ is closest to the optimum estimated

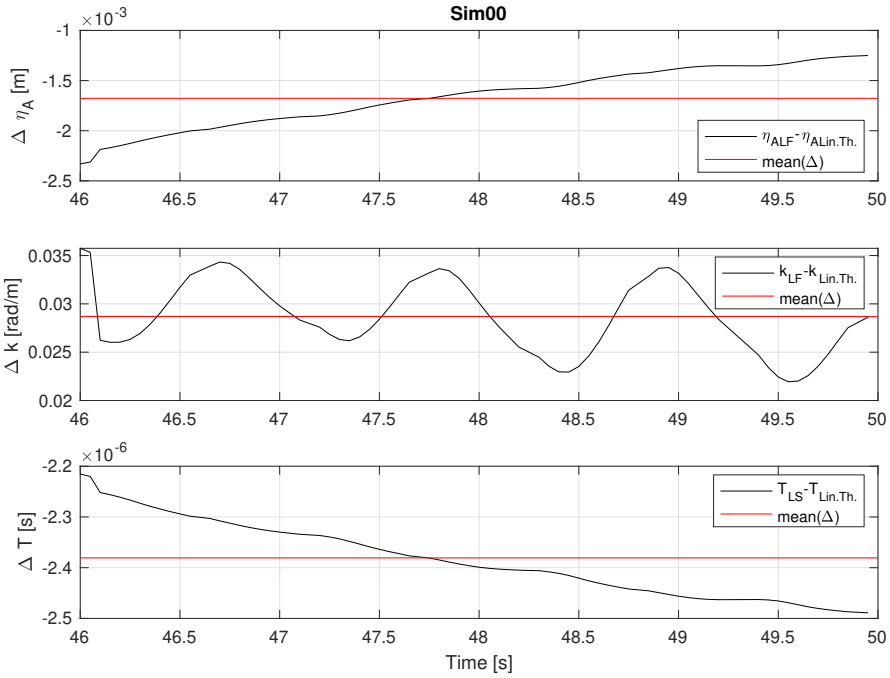

Figure 4: The temporally variation of the absolute error of the identified parameters related to the linear wave maker theory based values

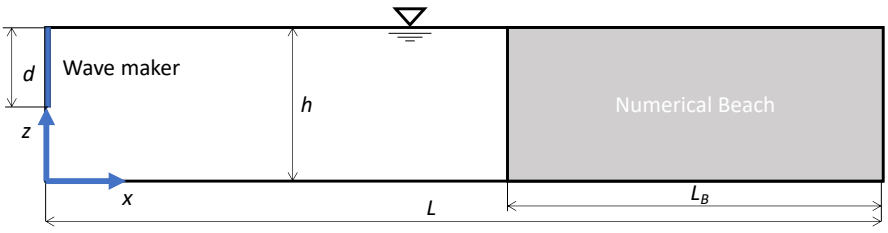

Figure 5: The two dimensional schematic representation of the numerical domain

Simulation nr.	NX	CFL	NZ	δ	Type
00	35	0.87	8	3.5	Basic setup
01	70	0.87	8	3.5	
02	140	0.87	8	3.5	Horizontal grid
03	17	0.87	8	3.5	size
04	9	0.87	8	3.5	
11	35	0.44	8	3.5	
12	35	0.22	8	3.5	Time step
13	35	1.75	8	3.5	
21	35	0.87	8	4.5	Stretching
22	35	0.87	8	2.5	factor
31	35	0.87	16	3.5	
32	35	0.87	22	3.5	Vertical grid size
33	35	0.87	4	3.5	

Table 1: Overview of the simulations performed during the sensitivity study

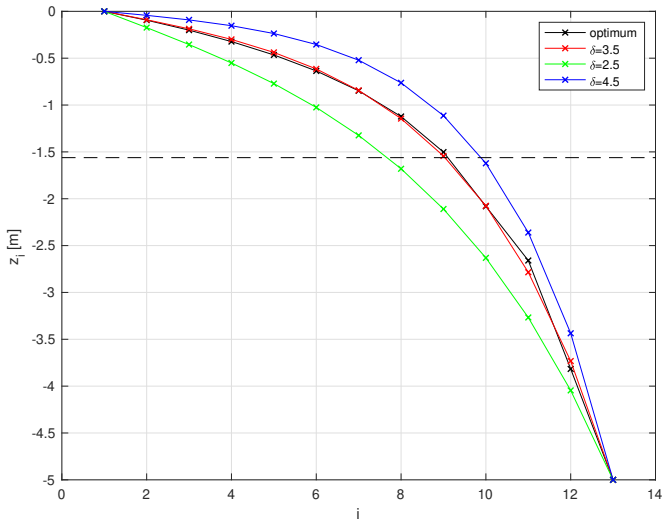

Figure 6: Vertical grid distribution in dependency on the stretching factor

using the presented method with the normalised error E equals 0.01.

The effect of the stretching factor can be observed in Figure 7. The top diagram of Figure 7a shows the recorded time series from the five simulations at 20 m distance away from the wave maker. As it takes time for the waves to propagate over this distance, one can see a transient phase at the arrival of the waves as a result of the initial ramp up of the wavemaker motions. It triggers a non-linear wave-wave interaction where the steeper waves catch the less steeper waves and the wave height increases Mei et al. (2005). The next diagram below with the Hilbert envelopes makes it easier to compare the time series. We can see a $2T$ oscillation,

due to the bounded waves in the envelopes, which makes the waves non-symmetric: the crest height is larger than the trough. This non-symmetry is reflected as a high frequency oscillation in the Hilbert envelopes. Both diagrams show that the wave amplitude is not influenced by the stretching factor. The results from the Fourier analysis (FA) are shown in the lowest two diagram of Figure 7a also supports this observation. The left hand side diagram shows the time window where the FA is applied and the right hand side diagram shows the amplitude spectrum. We can see peaks at $f_1 = 1.00$Hz and at $f_2 = 2.00$Hz which corresponding to the frequency of the free wave at $T = 1.00$s and the bounded wave frequency at $f_2 = 2f_1$. The amplitudes of the time series are almost the same.

The Hilbert envelope also shows that the simulated waves with $\delta = 2.5$ propagate the slowest. The different wave phase velocity causes a significant phase difference of the waves at $x = 20$ m. Correspondingly, the correlation coefficient is near minus one for most part of the chosen time window, indicating a near π phase difference in comparison to the simulation with $\delta = 3.5$. It is also observed from the Hilbert envelope that the simulated waves propagate faster with a stronger stretching factor $\delta = 4.5$. However, the phase differences between $\delta = 4.5$ and the $\delta = 3.5$ is not as significant as that between $\delta = 2.5$ and $\delta = 3.5$. The correlation coefficient is also seen to be near but smaller than 1.

In order to get a better overview of the results of the simulation, the mean value of the Hilbert envelopes and the mean value of the correlations in the FA's time windows are estimated at three locations and presented as bar diagram in Figure 7b. The black line in the upper diagram presents the expected wave amplitude value based on the linear wave maker theory and calculated from the maximum of the horizontal motion of the wavemaker flap motion S at the MWL:

$$\frac{A}{S} = 2\left(\frac{\sinh(k_p h)}{k_p d}\right)\frac{\cosh\left(k_p(h-d)\right) + k_p d\sinh(k_p h) - \cosh(k_p h)}{\sinh(2k_p h) + 2k_p h} \tag{39}$$

where the parameters h and d are defined in Figure 5 and k_p is the wave number of the propagating waves. As the diagram shows the variation of the stretching factor has not significant effect on the wave amplitudes, they are in good agreement with the linear theory proposed amplitude. The lower diagram shows the correlation of the time series against the stretching factor $\delta = 3.5$ simulation. The mean value of the correlation coefficient varies with the distance from the wave maker. The largest spatial variation of the correlation can be observed for the smallest stretching factor.

The choice of the optimal stretching factor that yields the correct dispersion relationship can be concluded from the lower diagram of Figure 8. The diagram shows the absolute errors of the wave numbers (Δk) in relation to the theoretical wave number estimated from the linear dispersion defined in Eqn. (17). The wave numbers estimated from both the least square (LS) method and the Fourier analysis (FA) of the free surface elevation are plotted together. It is seen that the stretching factor 3.5 gives the smallest error from both LS and FA estimations. The upper diagram, based on the analysis of the spatial results shows the same tendency as one can conclude from the result based on the time series analysis, that the variation of the stretching has not significant effect on the wave amplitude.

The position of the time windows is adjusted regarding to the distance to the wave maker and to the wave phase velocity.

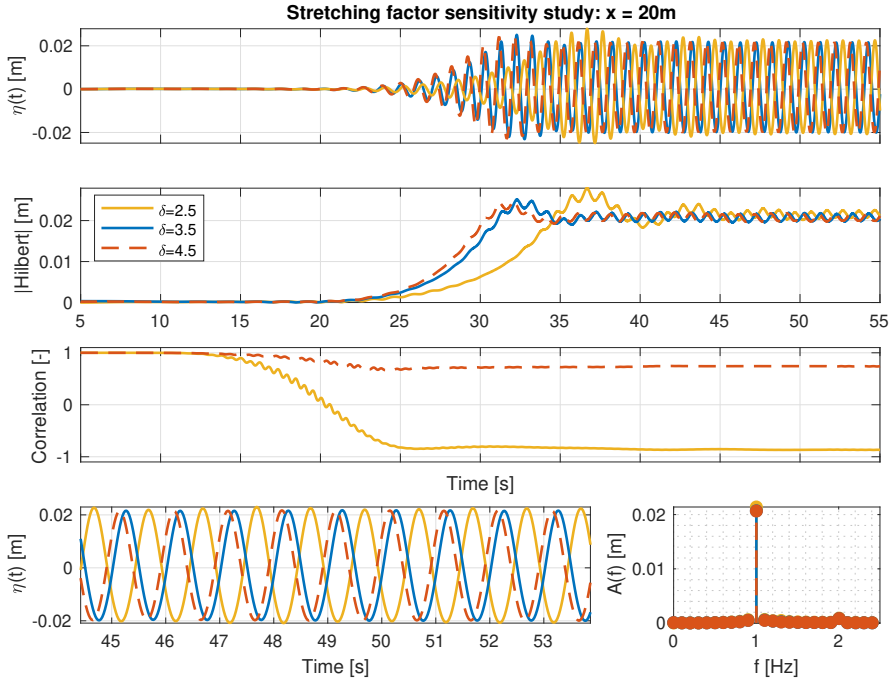

(a) $x = 20$m

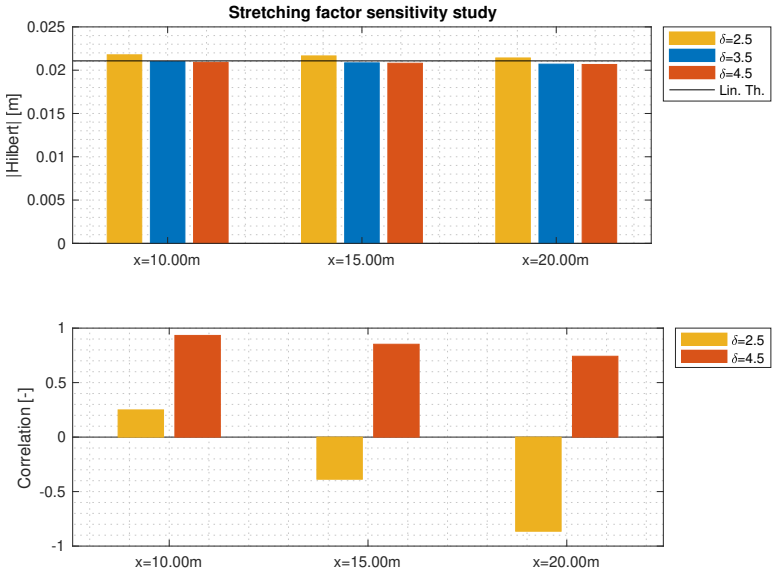

(b) Comparison at $x = 10, 15$ and 20m

Figure 7: (a) Times series of surface elevation, correlation coefficients and wave spectrum at $x = 20$ m using different stretching factors. (b) Comparison of the Hilbert envelope and correlation coefficients at $x = 10, 15$ and 20 m with different stretching factors.

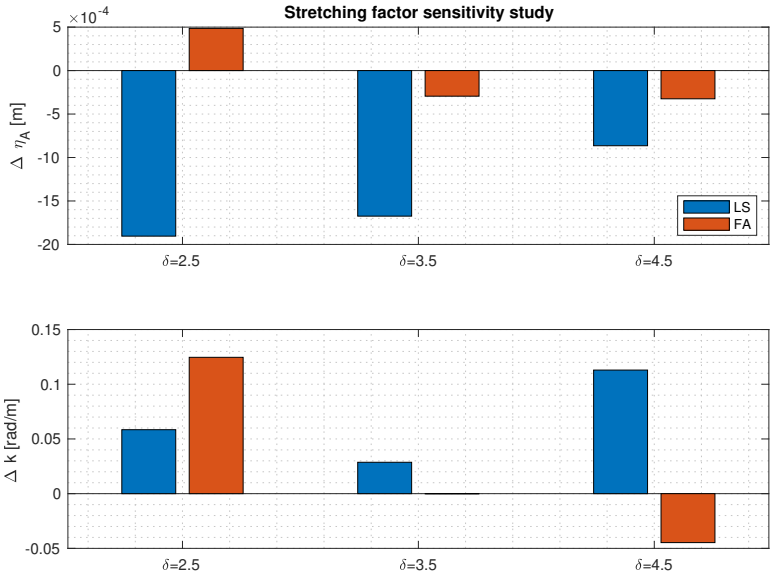

Figure 8: Overview of the stretching factor sensitivity study based on the spatial data using least square method (LS) and Fourier analysis (FA)

In the following sensitivity study of horizontal grid number (NX) and CFL number, the stretching factor $\delta = 3.5$ is used. For the sensitivity study of the number of the vertical grid point (NZ), a new optimal stretching factor is identified following the above methodology for each NZ.

The overview bar diagrams of all sensitivity studies based on the time domain analysis are presented in Figure 9. The horizontal grid spacing variation shows that it is necessary to use at least 35 grid point resolution per wave length to achieve good agreement with the linear theory regarding to the ave amplitude (Figure 9a). The correlation is already quite high, almost one for $\lambda/dx = 17$ where the wave amplitude not yet converged.

Using the optimal stretching for a given vertical grid resolution where the number of the grid points is at least eight guarantees a good wave phase velocity as is demonstrated in the lower diagram of Figure9a. The variation of the wave amplitude due to the change of the vertical grid resolution is much less than one can observe at the horizontal grid resolution. The variation of the time step has larger effect on the wave amplitude than on the wave propagation based on the comparison of the bars in Figure 9d.

5 Validation

5.1 Model test setup

An overview of the waves used in the validation is listed in Table. 2. The experiment was carried out in the long wave flume at Marintek (TANK I+III), Trondheim, Norway Onorato et al. (2005). The length of the tank is 260 m and the width is 10.5 m as shown in the figure. The depth of the tank is 10 m for the first 85m and 5.6 m for the rest of the flume. However, the sudden change from 10 m to 5.6 m is insignificant for the waves of 2.0 s and 1.5

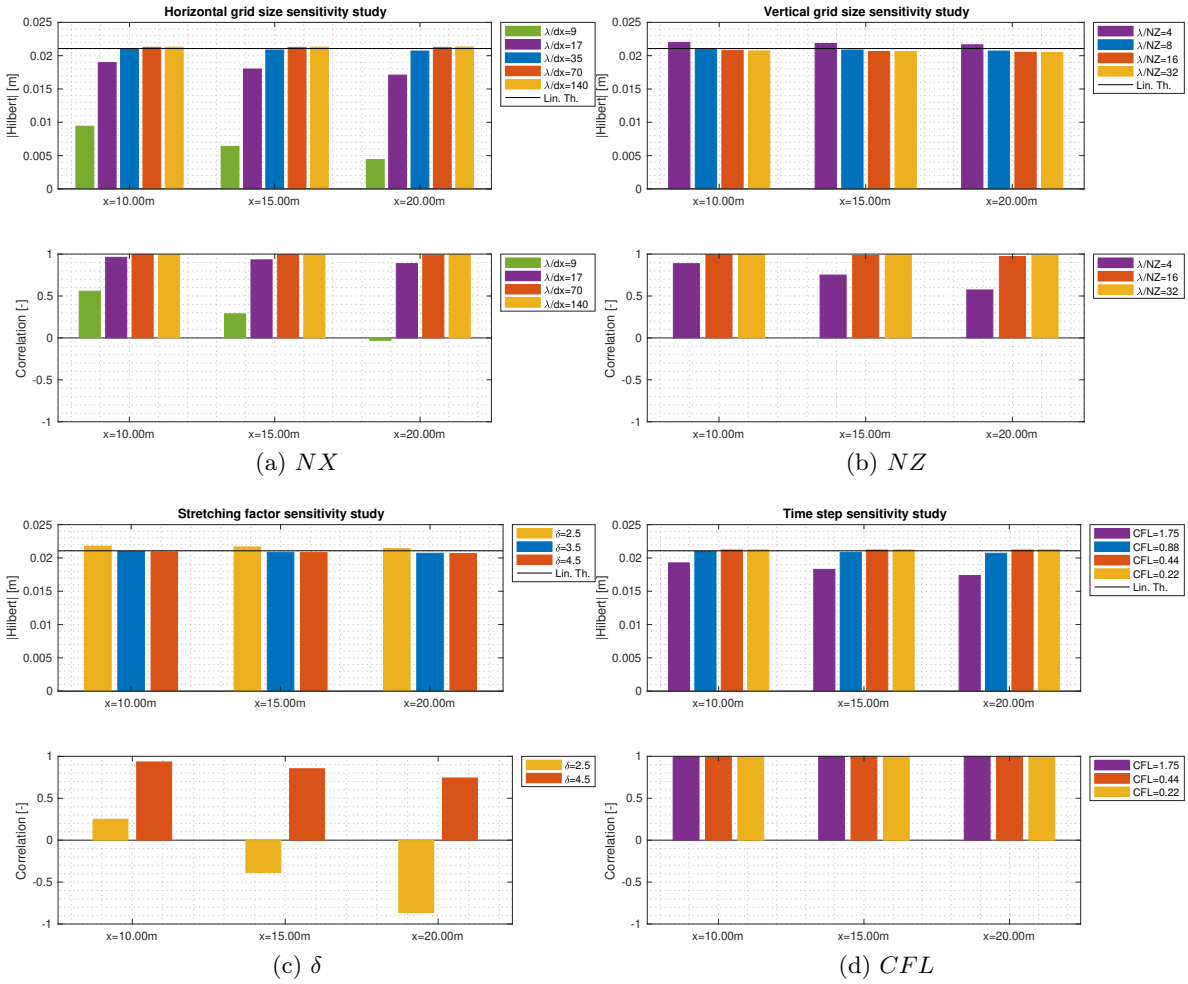

(a) NX (b) NZ

(c) δ (d) CFL

Figure 9: Sensitivity studies of the number of horizontal grid point NX, the number of vertical grid point NZ, the stretching factor δ and the CFL number.

s considered here. A horizontal double-hinged flap type wave-maker located at one end of the tank is used to generate the waves. The motion of the flaps are recorded during the tests. The free surface elevation is measured simultaneously by 19 probes placed at different locations along the flume. Twin-wire conductance measuring probes were used, with a 40 Hz sampling frequency. The locations of the wave probes are given in Figure 10. The wave homogeneity is controlled at two distances from the wave maker at $x = 75$m and $x = 160$m in ± 2 m distance from the central line of the flume. Here, in order to avoid unwanted reflection and ensure wave quality, only the first ten locations up to $x = 80$ m are used for the validations. The recorded time series of the flap motion are used in the simulation to generate the wave using REEF3D double-hinged flap type wave-maker model.

Test nr.	T [s]	H [m]		Wave theory
8900	2.0	0.1		2nd-order Stokes wave
8101	2.0	0.25		2nd-order Stokes wave
S18	2.0	0.78		5th-order Stokes wave

Test nr.	T_1 [s]	T_2 [s]		
8203	1.6	2.1		Bi-chromatic wave
8205	2.0	2.1		Bi-chromatic wave

Test nr.	T_1 [s]	T_2 [s]	T_3 [s]	
8300	1.365	1.500	1.667	Tri-chromatic wave

Test nr.	T_p [s]	H_s [m]	γ [-]	
8450	1.5	0.100	1.0	Irregular wave

Table 2: Input wave parameters for all validation cases

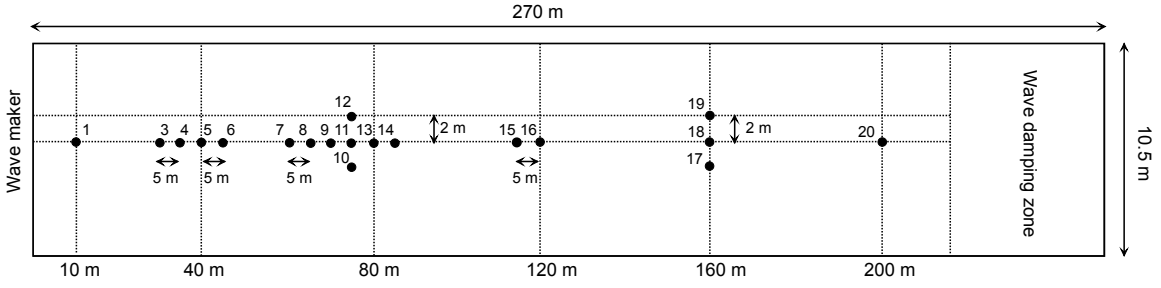

Figure 10: Location of the wave probes with the horizontal dimension of the flume (Onorato et al., 2005).

It was used 5.6 m water depth to calculate the $h/g\tau^2$ in the figure showing the wave are still deep water waves

5.2 Simulation setup

Based on the sensitivity studies in section 4, the setup of the simulation nr. 00 in section 4 is used in all of the rest simulations regarding to the horizontal uniform grid spacing ($\lambda/dx = 35$), time step ($dt = 0.88dx/c_{ph}$) and the number of vertical grid point per wave length ($NZ = 8$), if it is not mentioned otherwise. The vertical stretching is defined from a file by the normalised optimum vertical coordinates of the grid points for each simulation. This way it is not necessary to identify a stretching factor with a corresponding vertical grid point number for the sinh stretching method which is equivalent to the optimum vertical grid distribution.

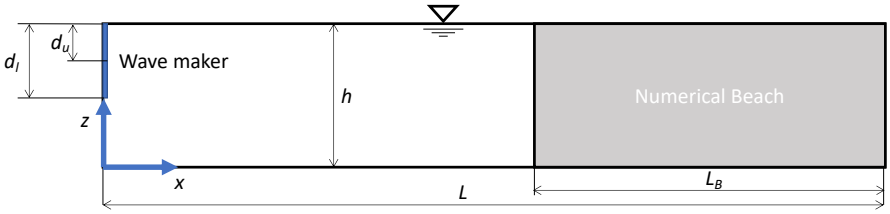

Figure 11: The two dimensional schematic representation of the numerical domain

The numerical domain length is set to $L = 250$m, the length of the numerical beach is $L_B = 30$m. The water depth is set to $h = 10$m according to the model test. The vertical location of the lower hinge of the wave maker d_l is 2.62 m below MWL and the upper hinge d_u is 1.05 m under MWL. The simulation is 2D with one layer of cells in the y-direction. The definition of these parameters and the applied coordinate system are presented in Figure 11. The free surface elevation is analysed at ten locations at the same distance away from the wave maker as in the model tests (Figure 10).

5.3 Regular waves

As mentioned earlier in the model test description, two regular waves with the same period of 2 s but different steepnesses are investigated. Though the proposed method considers only wave period and water depth as input and applies linear wave theory, the test is chosen to show its general applicability for waves of different steepnesses. The optimal vertical grid arrangement estimated using the proposed method is presented in Figure 12. It is clearly seen that the grid height changes significantly within one wave length below the still water level. At deeper depth than one wavelength, the vertical grid size does not change much.

The free surface time series, Hilbert envelopes, correlation coefficients and amplitude spectra from the simulations of the two regular wave simulations CO8900 and CO8101 are summarised in Figure 13 and Figure 14. The Hilbert envelopes of these time series show a good agreement between the simulations and the experiments regarding the magnitude of the time series after the waves propagated 75 m from the wave maker. The correlation curves, which quantify the similarity between the experiment and the simulations show that the numerical simulations are in phase with the model test record. The lower diagrams show the time windows where the Fourier analysis is applied and its results in the form of an amplitude spectrum at four different locations. The bar diagrams in Figure 15 give an overview of the

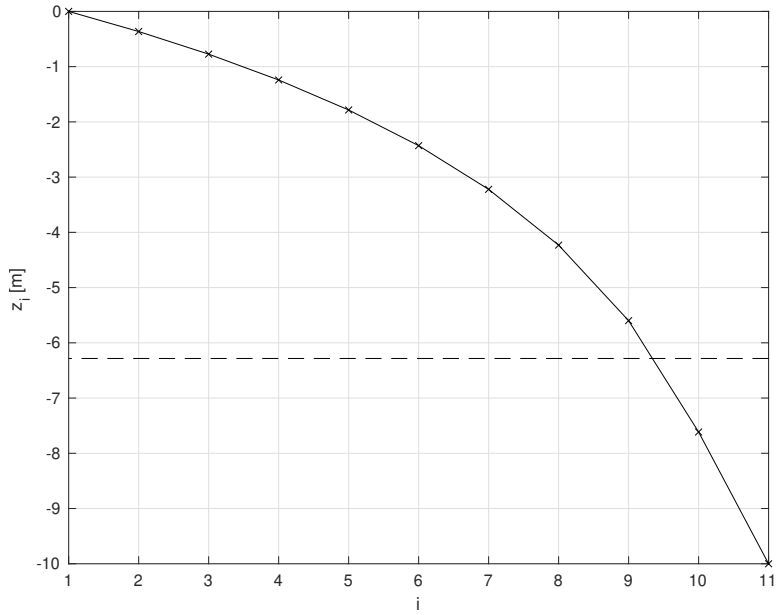

Figure 12: The applied vertical grid spacing for the regular wave validation.

average of the Hilbert envelopes in the upper diagrams and the average correlations in the lower diagrams at nine locations for both regular waves. It is seen that the wave propagation is stable throughout a tank during the simulation. No numerical dissipation and reduction of the mean wave amplitude are observed even at a long distance from the wavemaker. Based on this overview, one can conclude that the two simulations with the same vertical grid distribution give about the same accuracy regrading the magnitude and phase in spite of the different wave steepness.

For higher than 2nd-order nonlinear regular waves, the dispersion relationship changes and thus the calculation of wave number needs to be updated in the proposed method. In order to demonstrate the applicability of the proposed method for steep waves, an additional case S18 is investigated in addition to the model test cases. The tested wave is a 5th-order Stokes wave with the same wave period of 2 s but an increased wave height of 0.78 m, resulting in a wave steepness $H/\lambda = 0.125$. The computational domain and water depth are kept the same as the model test cases, a relaxation zone Mayer et al. (1998) is used to generate the waves since there is no wavemaker inputs for this case. The vertical grid arrangement is shown in Fig. 16 with the wave number calculated based on Fenton's Stokes wave theory Fenton (1985). The time series of the free surface elevation at $x = 75$ m is compared to the theoretical calculations, as shown in Fig. 17. It is seen that a very good agreement of wave height, phase velocity and correlation is achieved using the proposed method for this steep nonlinear wave.

5.4 Bi-chromatic waves

The simplest irregular sea state is bichromatic waves where the free waves consist of only two different wave periods. This kind of sea states are often used to investigate non-linear wave-wave interactions. An incorrect representation of the dispersion relation leads to incorrect non-linear wave-wave interactions patterns, for example wave focusing at the wrong loca-

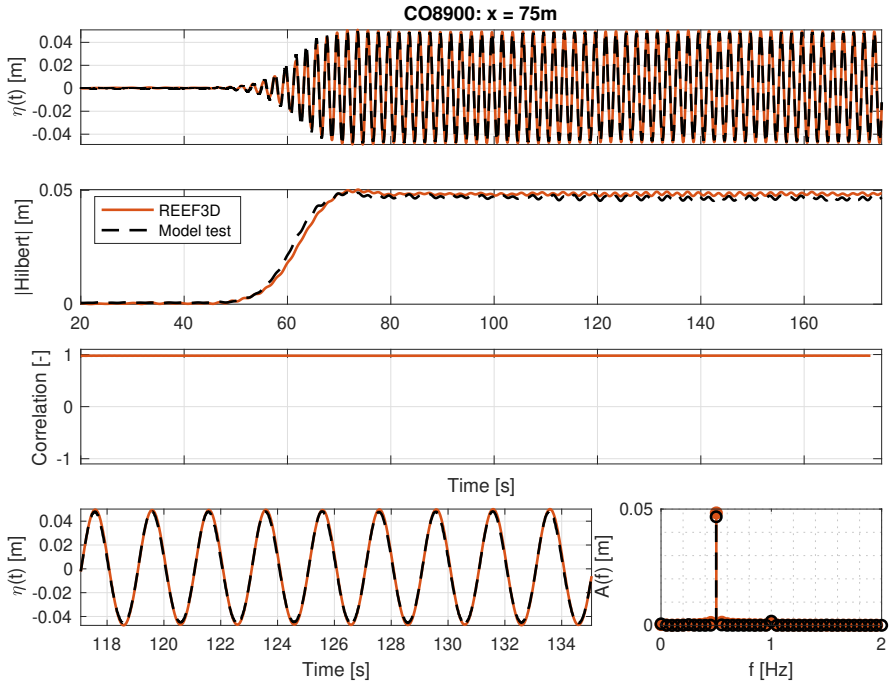

Figure 13: Validation of the test nr.: CO8900 at x =75 m.

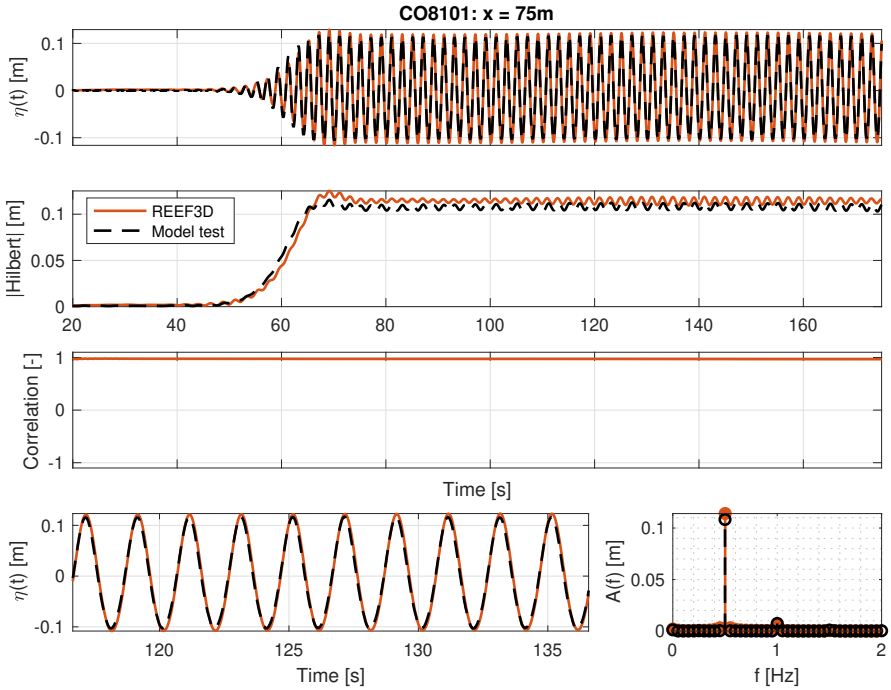

Figure 14: Validation of the test nr.: CO8101 at x =75 m.

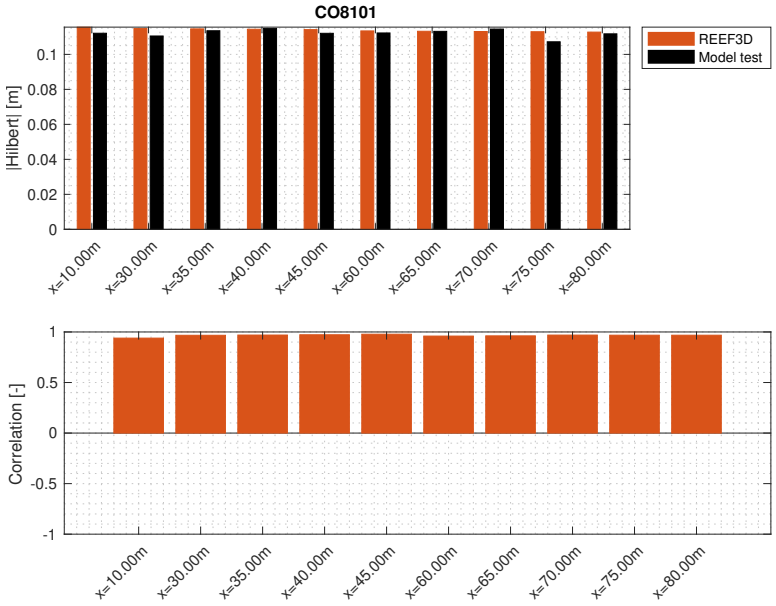

Figure 15: Comparison of the mean values of the time series at all wave gauges for case CO8101.

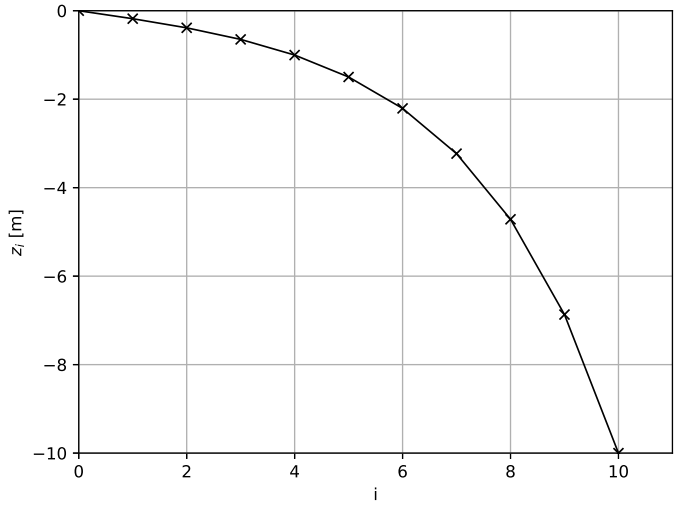

Figure 16: The applied vertical grid spacing for the 5th-order Stokes regular wave with a wave steepness $H/\lambda = 0.125$.

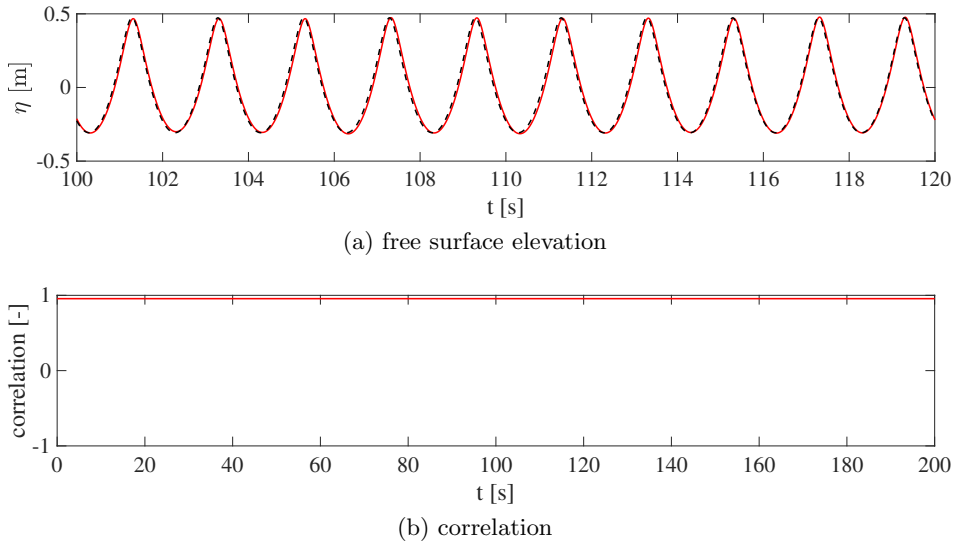

(a) free surface elevation

(b) correlation

Figure 17: Validation of the 5th-order Stokes regular wave with a wave steepness $H/\lambda = 0.125$. The time series at wave gauge $x = 75$ m is compared to the Stokes wave theory in (a) and the correlation between the simulated and theoretical free surface is shown in (b).

tions. Therefore, it is important that both free wave components are correctly represented. However, it is not possible to calculate an optimal vertical grid distribution that satisfied both frequencies at the same time based on Eqn. (21). In this case, the optimal distribution is calculated for each frequency and the following procedure is adopted to combine them these two distributions

1. Define an optimal grid-spacing for the shorter wave component with at least eight vertical grid points per wave length below the still water level
2. Search for a constant truncation error value that produces a vertical-spacing that closely resembles the one from the previous step for the longer wave component
3. Combine the grid spacing for the shorter wave component within one wavelength below the still water level with the grid spacing for the longer wave component for the rest of the water depth.

The combination process focuses highly on the grid distribution within one wavelength below the still water level. as this region is the most critical for the determination of the dispersion relation and phase velocity. The result of such mixed grid-distribution for the bichromatic wave of test nr. CO8203 is shown in Figure 18. The black crosses present the optimal grid-spacing for the shorter wave $T = 1.6$s. The blue crosses show the location of the vertical grid points for the longer wave $T = 2.0$s which are the closest to the black crosses up to the deep L_1 which is the wave length of the wave with period 1.6 s. The red diamonds show the mixed grid locations which is used in the simulation.

The free surface time series, wave spectrum and Hilbert envelope are compared between the simulation and the model test in Figure 19 together with their correlation coefficients.

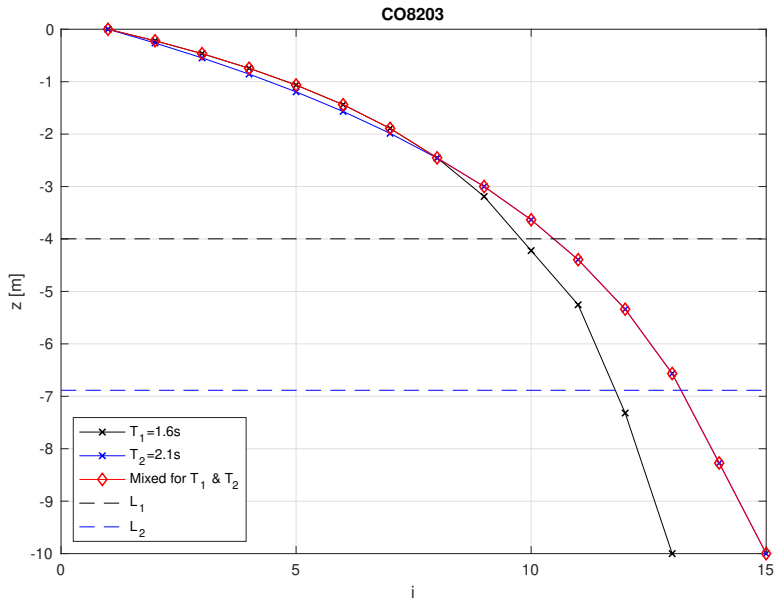

Figure 18: The applied vertical grid spacing for the bichromatic wave CO8203

The comparison of the time series shows a good agreement both in terms of amplitude and phase at all locations in Figure 19a. The numerical simulation also represents all frequency components in the wave spectrum, including the high frequencies from the bounded waves due to wave-wave interactions. The correlation between the simulated free surface and the model test is nearly constant after $x = 30$ m, as seen in Figure 19b. This shows a high-quality representation of the wave field even at a long distance away from the wavemaker.

For the other tested bichromatic wave, the wave periods of the two components are very close to each other, which makes it easier to combine the grid spacings. The time series of the experiment and the numerical simulation are compared in Figure 20. Similarly, both the amplitudes and wave phase are in good agreement between the simulation and the physical test. The Hilbert diagram shows only minor differences and the correlation coefficients are stably near one for the distance larger than 30 m from the wavemaker. There are few high-frequency components in the wave spectrum for both the simulation and model test due to the different composition of the wave frequency.

In this section, the proposed method is extended to determine the optimal vertical grid arrangement for a wave field with more than one frequency component. Through the validations, the extended method demonstrates high effectiveness and contributes to a high quality numerical reproduction of a bichromatic wave field.

5.5 Tri-chromatic wave

The same approach used to find the optimal vertical grid distribution for a bichromatic wave is applied in the section to ermine the grid arrangement for a trichromatic wave. In this case, the optimal solution needs to take into account three wave lengths. In short, the combined σ-grid for the chosen trichromatic wave is demonstrated in Figure 21. The black crosses present the grid spacing for the shortest wave, the green crosses for the longest and the blue

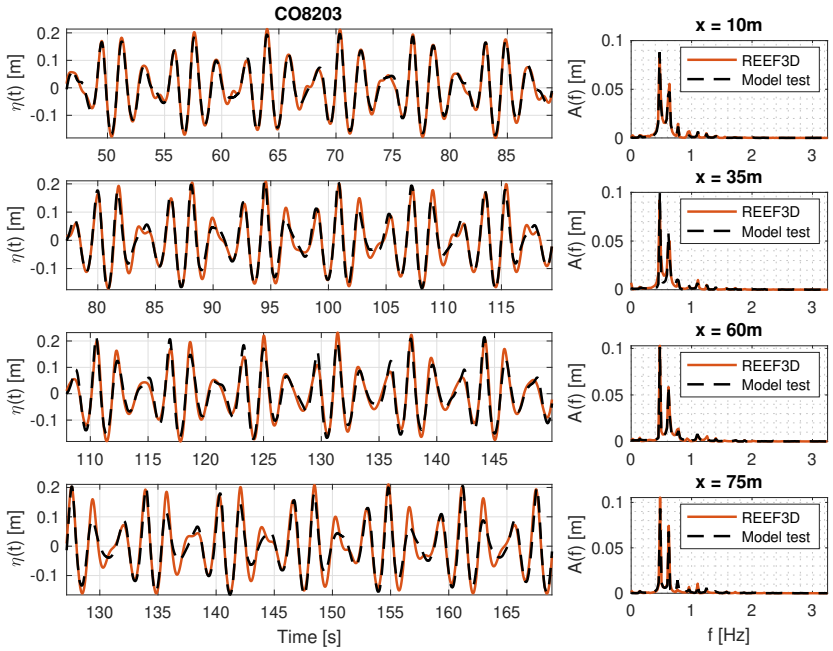

(a) Fourier Analysis

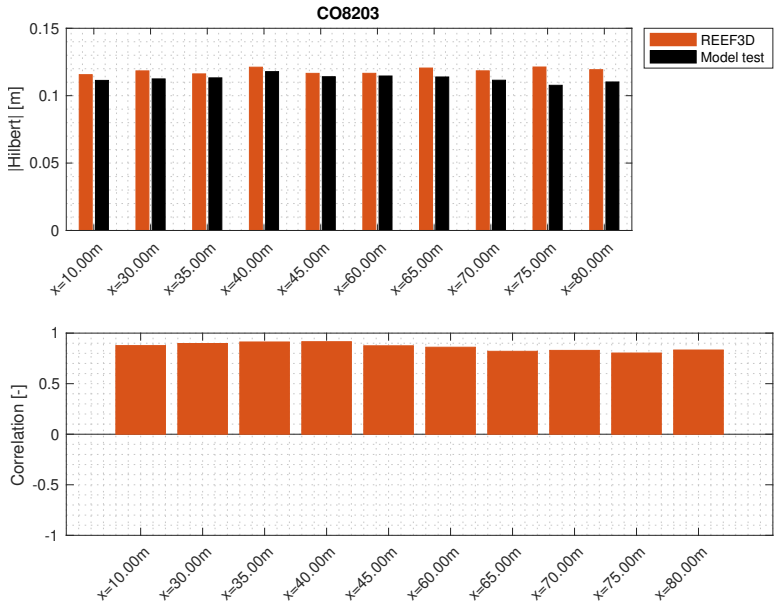

(b) Comparison of the mean values

Figure 19: Validation of the bichromatic wave case CO8203.

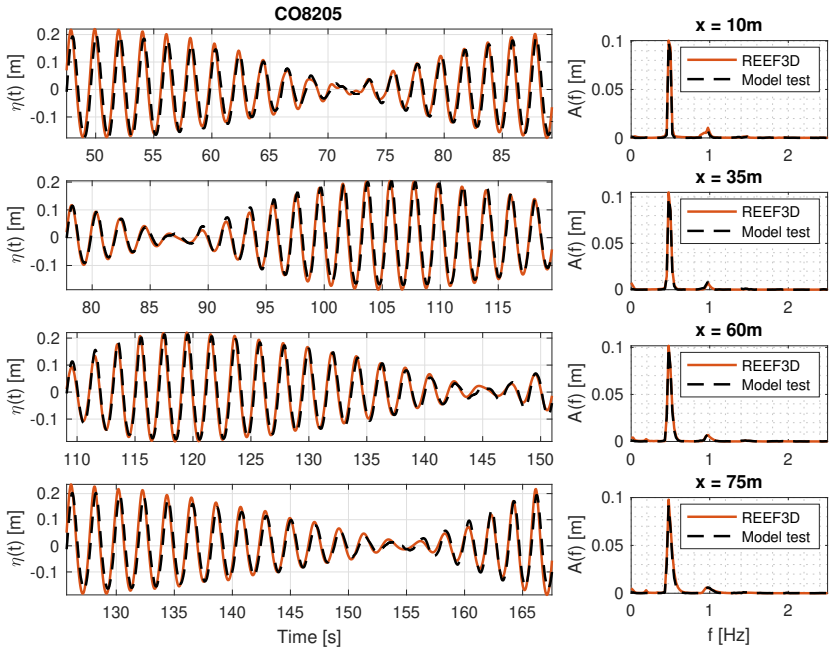

(a) Fourier Analysis

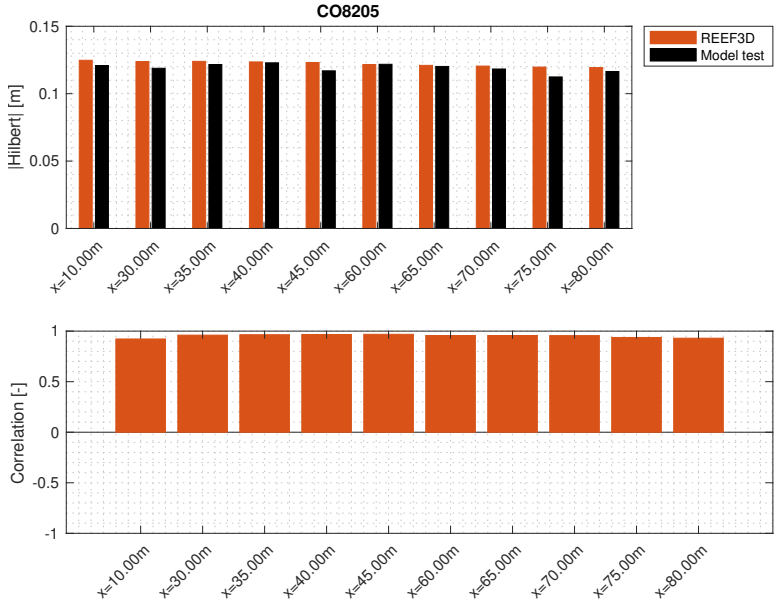

(b) Comparison of the mean values

Figure 20: Validation of the bichromatic wave case CO8205.

crosses for the wave with wave period equals to 1.5 s. The cyan diamonds show the vertical spacing for the two shortest wave and the red diamonds is the final location of the grid points.

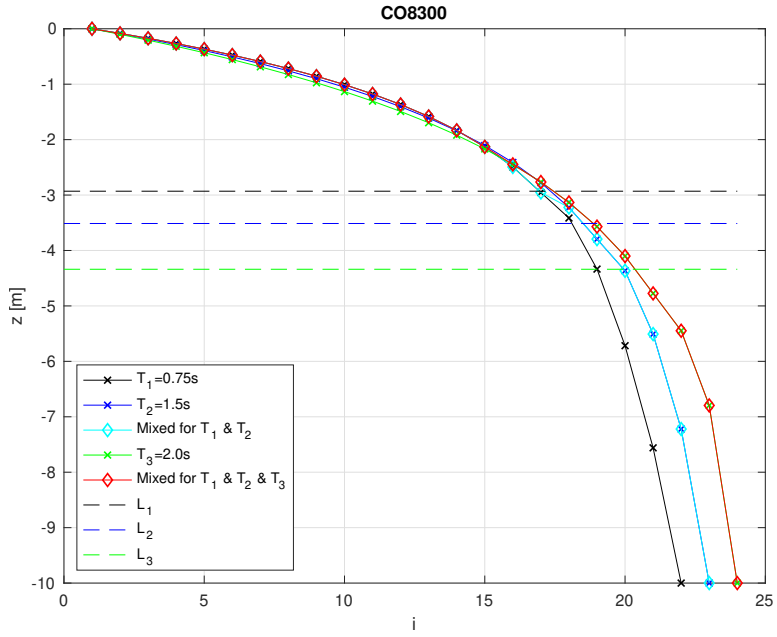

Figure 21: The applied vertical grid spacing for the trichromatic wave CO8300

The simulated free surface time series and statistics are compared with the model test data in Figure 22. The overall accuracy of the simulation of the trichromatic wave is satisfactory, the time series represent the correct wave amplitudes and are in phase with the measurements. The wave spectrum from the simulation also represents all the frequency components at all measured locations. The evolution of the time series also shows a gradual focusing due to nonlinear wave-wave interaction, which results in a very steep wave crest at $x = 75$ m. This extreme event is also well represented in the simulation. Both the crest height and the focusing location align with the measured data. It is noticed that the Hilbert envelope of the model test data shows a slight but steady decrease with distance after $x = 40$ m, which results in the corresponding decrease of the correlation values. The discrepancy is likely due to the different methods used in the wave damping zone towards the end of the wave tank.

5.6 Irregular Sea State

A 3-hour full scale simulation of an irregular sea state prescribed by a JONSWAP spectrum is performed in this section. The theoretical JONSWAP spectrum and the target spectrum measured in the physical model test are shown in Figure 23a. In the physical model test, the random phase and random amplitude method are used to generate the target time series, from which the target spectrum is constructed. As a result, the target spectrum is different from the theoretical spectrum. The low-end, high-end and peak frequencies of the chosen frequency band are the most important frequencies in consideration. These three frequencies

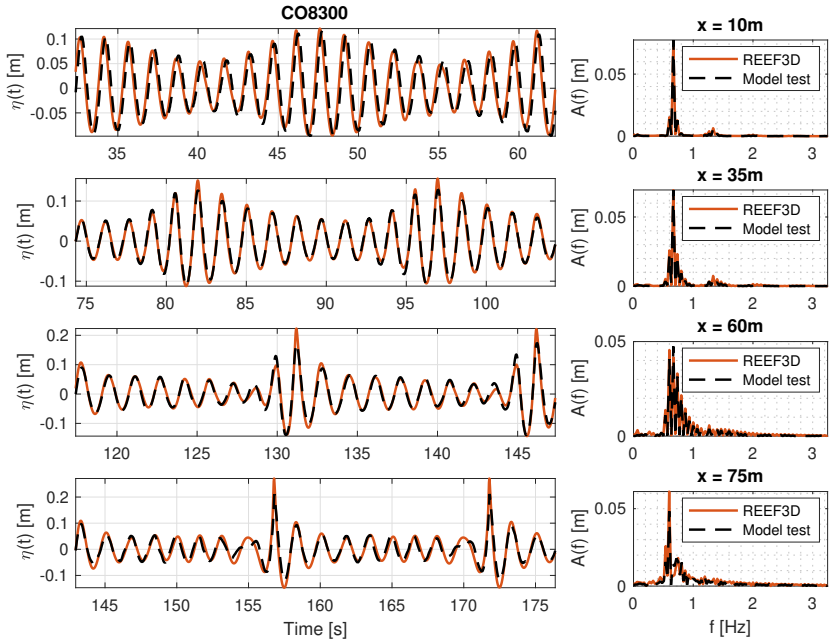

(a) Fourier Analysis

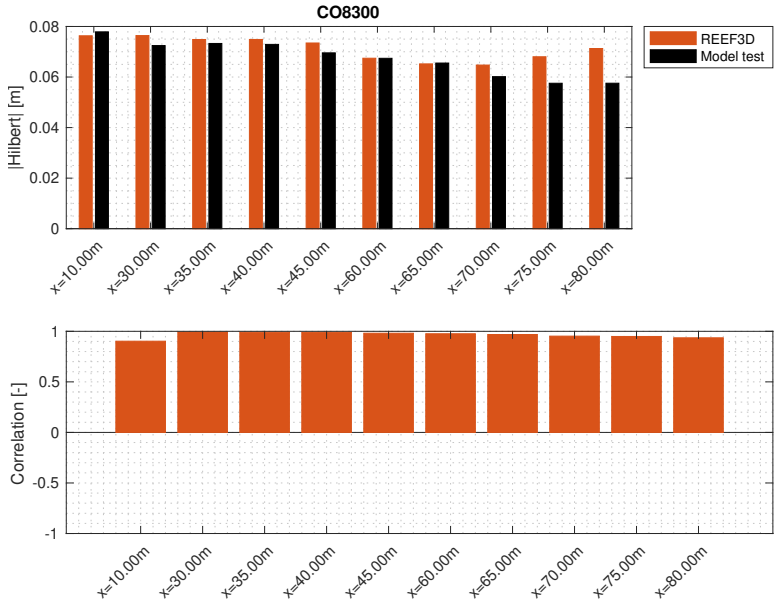

(b) Comparison of the mean values

Figure 22: Validation of the trichromatic wave simulation of case CO8300.

are indicated with green, black and blue vertical dashed lines in Figure 23a. As a result, the procedure to determine the optimal vertical grid arrangement for an irregular wave is very similar to that for a trichromatic wave. The optimal arrangement for each frequency and combined frequencies are summarised in Figure 21.

The simulated free surface time series and the correlation diagrams are compared with the model test measurements in Figure 24. The convolution window's size of the correlation analysis is set to be three times of the peak periods. It is seen that the correlation coefficient is above 0.85 most of the time, which indicates an overall good agreement with the measured experimental data. Some of the extreme wave events are extracted from the time series and close examinations are illustrated in Figure 25. The time series at the extreme events also show good agreement with the measured data and the correlation coefficients near the extreme waves are generally above 0.9, indicating a correct representation of both the magnitude and phase of the simulated waves. This observation shows that the proposed method is able to produce steep nonlinear waves in an irregular wave field with high accuracy.

The reconstructed wave spectra are also compared for the simulation, model test and theory, as shown in Figure 26. The peak frequency and the spectrum peaks from the simulation agree very well with the model test. The spectrum shape over the chosen frequency band also shows good agreement, including high frequency range. However, it is also observed that there is a slight overestimation of wave energy between the peak frequency and the high-end frequency as waves propagate further than 35 m from the wavemaker. This could be possibly caused by insufficient damping of the breaking waves in the simulation. In addition, it is also more challenging to optimize the vertical grid arrangement that is suitable for all wave components when the difference between the smallest wave number (lowest frequency) and the largest wave number (highest frequency) is significant, which is usually the case with sea states at deep water conditions. This challenge is less prominent for intermediate and shallow water conditions where the wave propagation velocity of the wave components is closer to each other.

The validation of the 3-hour irregular wave simulation shows that the proposed method contributes to a satisfactory representation of irregular sea states.

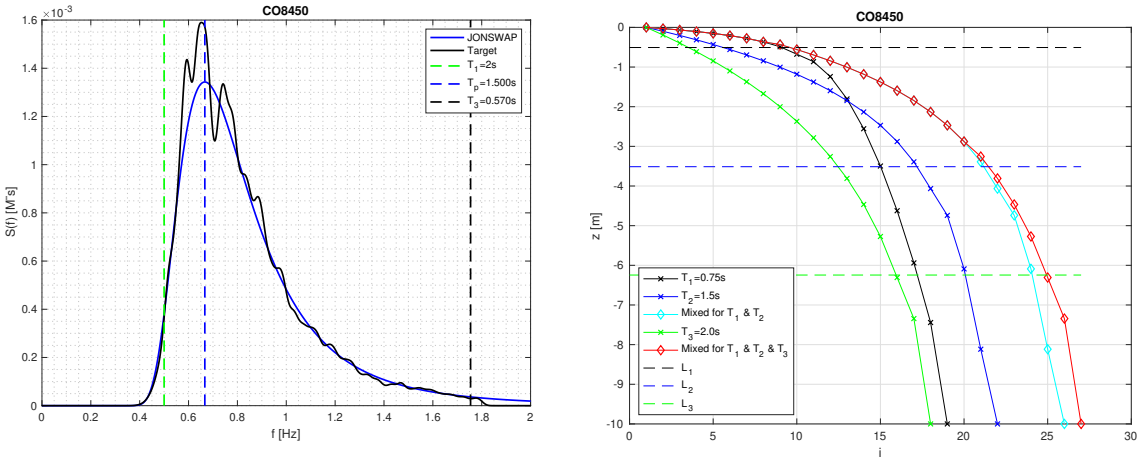

(a) Theoretical spectrum (b) Applied vertical displacements of the σ-grid

Figure 23: (a)The input spectrum, the dashed green, blue and black vertical lines indicate the low-end frequency, peak frequency and high-end frequency for the chosen frequency band. (b) The applied vertical grid. The green, blue and back curves with cross markers are optimised vertical grid arrangements for the low-end frequency, peak frequency and high-end frequency. The cyan and red cores with diamond markers are optimised vertical grid arrangements considering the peak frequency and the high-end frequency and considering all frequencies.

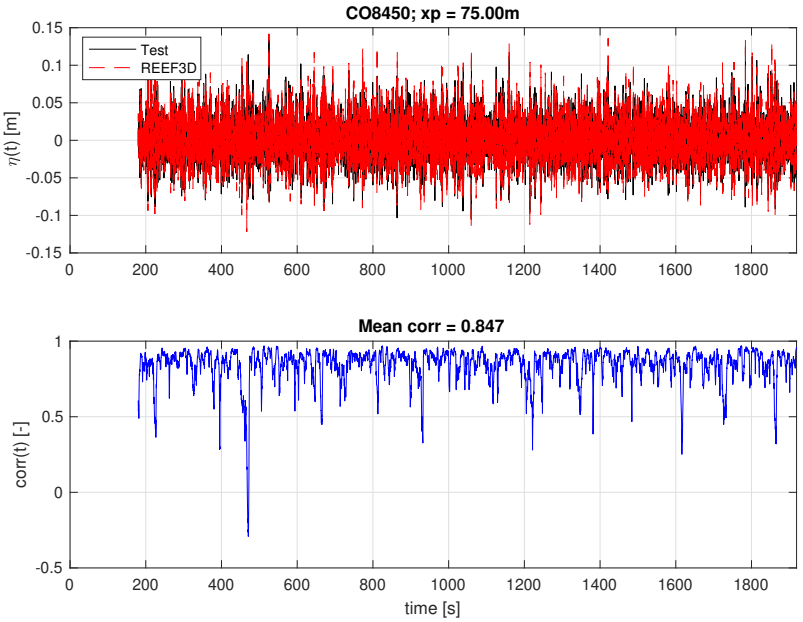

(a) $x = 75$m

Figure 24: Time series and correlation coefficients for the entire simulation duration at $x = 75$ m in the irregular wave simulation.

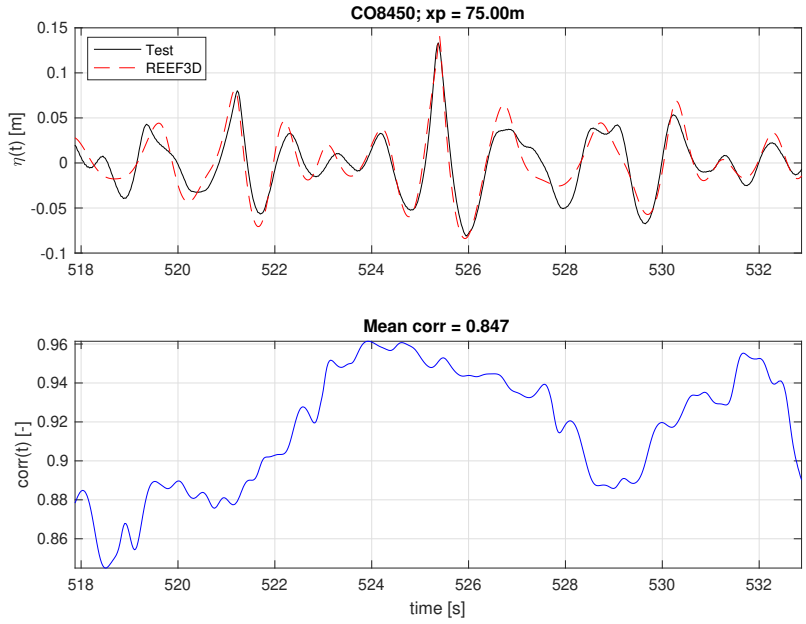

(a) $x = 75$m

Figure 25: Comparison of the time series and correlation coefficients for the extreme events at $x = 75$ m in the irregular wave simulation.

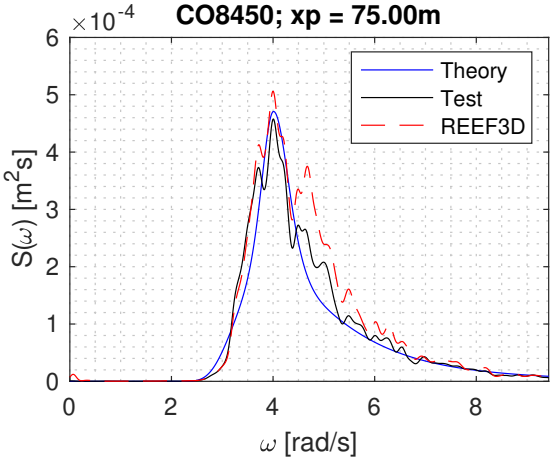

(a) $x = 75$m

Figure 26: Comparison of the spectrum, RAO, Coherence and phase information at $x = 75$ m for the irregular wave simulation.

6 Conclusions

The choice of the vertical σ-grid arrangement in a nonlinear potential flow wave model has a significant impact on the phase error of the simulated waves. A novel method to optimise the vertical grid arrangement is presented in this article to minimise the errors in the dispersion relation and maximise the advantage of the σ-grid and grid stretching. By keeping a constant truncation error in the vertical direction of the velocity potential, the coordinates of the vertical grid points for the correct representation of wave number can be calculated, based on the number of grid points and the order of the finite difference scheme. This new truncation error based methodology together with its practical implementation is demonstrated in a regular wave propagation simulation. The numerical results that are generated using the optimised vertical grid arrangement show very good representation of the wave phase velocity and significant improvements in comparison to other grid arrangements.

The novel method is used in the numerical wave tank of the fully nonlinear potential flow model REEF3D::FNPF and the simulated waves are validated against experimental measurements. Four scenarios are considered, regular wave, bichromatic wave, trichromatic wave and irregular wave. Correct phase information and spectrum are represented in all presented simulations and good agreement with the measured data is achieved. These simulations further prove the effectiveness and flexibility of the proposed method for different wave scenarios. From these validation cases, it is noticed that the proposed method is not only suitable for regular waves, but also for steep waves and waves that consist of many frequency components. The wave-wave interactions and the resulting extreme events in a multi-frequency wave field can also be well represented.

Acknowledgements

This work is part of the "High Resolution Numerical Modelling of Flexible Fish Cage Structures" project and the authors gratefully acknowledge the support from the Norwegian Research Concil (grant 267981). The authors are grateful to the model test data provided by the the Transnational Access to Research Infrastructures Program of the European Commission under the contract HPRI-CT-2001- 00176. The computations were performed on resources provided by UNINETT Sigma2 - the National Infrastructure for High Performance Computing and Data Storage in Norway.

Acknowledgements

This study has been carried out under the and the authors are grateful to the grants provided by

References

Aggarwal, A., Tomaselli, P.D., Christensen, E.D. and Bihs, H. (2020). Computational Fluid Dynamics Investigations of Breaking Focused Wave-Induced Loads on a Monopile and the Effect of Breaker Location. *Journal of Offshore Mechanics and Arctic Engineering*, **142**(2). ISSN 0892-7219. 10.1016/j.oceaneng.2021.10974110.1115/1.4045187.

Ahmad, N., Kamath, A. and Bihs, H. (2020). 3D numerical modelling of scour around a jacket structure with dynamic free surface capturing. *Ocean Engineering*, **200**, 107104. ISSN 0029-8018. 10.1016/j.oceaneng.2021.109741https://doi.org/10.1016/j.oceaneng.2020.107104.

Alagan Chella, M., Bihs, H., Kamath, A., Myrhaug, D. and Arntsen, Ø.A. (2019). Breaking Wave Interaction With a Group of Four Vertical Slender Cylinders in Two Square Arrangements. *Journal of Offshore Mechanics and Arctic Engineering*, **141**(6). ISSN 0892-7219. 10.1016/j.oceaneng.2021.10974110.1115/1.4043597.

Bihs, H., Kamath, A., Alagan Chella, M., Aggarwal, A. and Arntsen, Ø.A. (2016). A new level set numerical wave tank with improved density interpolation for complex wave hydrodynamics. *Computers and Fluids*, **140**, 191 – 208. ISSN 0045-7930. 10.1016/j.oceaneng.2021.109741http://dx.doi.org/10.1016/j.compfluid.2016.09.012.

Bihs, H., Wang, W., Pakozdi, C. and Kamath, A. (2020). REEF3D::FNPF-a flexible fully nonlinear potential flow solver. *Journal of Offshore Mechanics and Arctic Engineering*, **142**(4). ISSN 0892-7219. 10.1016/j.oceaneng.2021.10974110.1115/1.4045915.

Bingham, H.B. and Zhang, H. (2007). On the accuracy of finite-difference solutions for nonlinear water waves. *Journal of Engineering Mathematics*, **58**(1), 211–228. ISSN 1573-2703. 10.1016/j.oceaneng.2021.10974110.1007/s10665-006-9108-4.

Bonnefoy, F., Le Touzé, D. and Ferrant, P. (2006*a*). A fully-spectral 3d time-domain model for second-order simulation of wavetank experiments. part a: Formulation, implementation and numerical properties. *Applied Ocean Research*, **28**(1), 33 – 43. ISSN 0141-1187. 10.1016/j.oceaneng.2021.109741https://doi.org/10.1016/j.apor.2006.05.004.

Bonnefoy, F., Le Touzé, D. and Ferrant, P. (2006*b*). A fully-spectral 3d time-domain model for second-order simulation of wavetank experiments. part b: Validation, calibration versus experiments and sample applications. *Applied Ocean Research*, **28**(2), 121 – 132. ISSN 0141-1187. 10.1016/j.oceaneng.2021.109741https://doi.org/10.1016/j.apor.2006.05.003.

Bunnik, T. and de Ridder, E.J. (2018). Using nonlinear wave kinematics to estimate the loads on offshore wind turbines in 3-hour sea states. In: *ASME 2018 37th International Conference on Ocean, Offshore and Artic Engineering*. Madrid, Spain. OMAE2018-77807.

Chi-Wang, S. and Stanley, O. (1988). Efficient implementation of essentially non-oscillatory shock-capturing schemes. *Journal of Computational Physics*, **77**(2), 439–471.

Dean, R.G. and Dalrymple, R.A. (1991). *Water wave mechanics for engineers and scientists*, volume 2 of *Advanced series on ocean engineering*. Singapore ; Teaneck, NJ : World Scientific, ©1991.

Ducrozet, G., Bonnefoy, F.e.l., Le Touzé, D. and Ferrant, P. (2012). A modified High-Order Spectral method for wavemaker modeling in a numerical wave tank. *European Journal of Mechanics - B/Fluids*, **34**. 10.1016/j.oceaneng.2021.10974110.1016/j.euromechflu.2012.01.017.

Engsig-Karup, A.P., Bingham, H.B. and Lindberg, O. (2009). An efficient flexible-order model for 3D nonlinear water waves. *Journal of Computational Physics*, **228**, 2100–2118.

Engsig-Karup, A.P., Madsen, M.G. and Glimberg, S.L. (2012). A massively parallel gpu-accelerated model for analysis of fully nonlinear free surface waves. *International Journal for Numerical Methods in Fluids*, **70**(1).

Falgout, R.D., Jones, J.E. and Yang, U.M. (2006). Conceptual interfaces in hypre. *Future Gener. Comput. Syst.*, **22**(1-2), 239–251. ISSN 0167-739X. 10.1016/j.oceaneng.2021.10974110.1016/j.future.2003.09.006.

Fenton, D. (1985). A fifth-order stokes theory for steady waves. *J. Wtrway Port Coast. Oc. Eng*, 216–234.

Glimberg, L.S., Engsig-Karup, A.P., Nielsen, A.S. and Dammann, B. (2013). Development of software components for heterogeneous many-core architectures. In: R. Couturier (Editor), *Designing Scientific Applications on GPUs*, Lecture notes in computational science and engineering, 73–104. CRC Press / Taylor & Francis Group.

Grilli, S.T., Guyenne, P. and Dias, F. (2001). A fully non-linear model for three-dimensional overturning waves over an arbitrary bottom. *International Journal for Numerical Methods in Fluids*, **35**(7), 829–867.

Grilli, S.T., Subramanya, R., Svendsen, I.A. and Veeramony, J. (1994). Shoaling of solitary waves on plane beaches. *Journal of Waterway Port Coastal and Ocean Engineering*, **120**(6), 609–628.

Guang-Shan, J. and Chi-Wang, S. (1996). Efficient implementation of weighted eno schemes. *Journal of Computational Physics*, **126**(1), 202–228.

Kusumawinahyu, W.M., Karjanto, N. and Klopman, G. (2006). Linear theory for single and double flap wavemakers. *J. Indones. Math. Soc.*, **12**(1), 41–57.

Li, B. and Fleming, C.A. (1997). A three dimensional multigrid model for fully nonlinear water waves. *Coastal Engineering*, **30**(3), 235 – 258. ISSN 0378-3839. 10.1016/j.oceaneng.2021.109741https://doi.org/10.1016/S0378-3839(96)00046-4.

Martin, T., Kamath, A. and Bihs, H. (2020). A lagrangian approach for the coupled simulation of fixed net structures in a eulerian fluid model. *Journal of Fluids and Structures*, **94**, 102962. ISSN 0889-9746. 10.1016/j.oceaneng.2021.109741https://doi.org/10.1016/j.jfluidstructs.2020.102962.

Mayer, S., Garapon, A. and Sørensen, L.S. (1998). A fractional step method for unsteady free-surface flow with applications to non-linear wave dynamics. *International Journal for Numerical Methods in Fluids*, **28**(2), 293–315. ISSN 1097-0363. 10.1016/j.oceaneng.2021.10974110.1002/(SICI)1097-0363(19980815)28:2¡293::AID-FLD719¿3.0.CO;2-1.

Mei, C.C., Stiassnie, M. and Yue, D.K.P. (2005). *Theory and Applications of Ocean Surface Waves*, volume 23 of *Advanced Series on Ocean Engieering*, chapter 1. World Scientific.

Onorato, M., Osborne, A., Serio, M. and Cavaleri, L. (2005). Modulational instability and non-gaussian statistics in experimental random water-wave trains. *Physics of Fluids*, **17**(7).

Onorato, M., Osborne, A., Serio, M., Cavaleri, L., Brandini, C. and Stansberg, C. (2004). Observation of strongly non-Gaussian statistics for random sea surface gravity waves in wave flume experiments. *Physical Review E*, **70**(6).

Raoult, C., Benoit, M. and Yates, M.L. (2016). Validation of a fully nonlinear and dispersive wave model with laboratory non-breaking experiments. *Coastal Engineering*, **114**, 194 – 207. ISSN 0378-3839. 10.1016/j.oceaneng.2021.109741https://doi.org/10.1016/j.coastaleng.2016.04.003.

Sasikumar, A., Kamath, A. and Bihs, H. (2020). Modeling porous coastal structures using a level set method based VRANS-solver on staggered grids. *Coastal Engineering Journal*, **62**(2), 198–216. 10.1016/j.oceaneng.2021.10974110.1080/21664250.2020.1734412.

Wang, W., Kamath, A., Pakozdi, C. and Bihs, H. (2019). Investigation of focusing wave properties in a numerical wave tank with a fully nonlinear potential flow model. *Journal of Marine Science and Engineering*, **7**(10). ISSN 2077-1312. 10.1016/j.oceaneng.2021.10974110.3390/jmse7100375.

Yates, M.L. and Benoit, M. (2015). Accuracy and efficiency of two numerical methods of solving the potential flow problem for highly nonlinear and dispersive water waves. *International Journal for Numerical Methods in Fluids*, **77**(10), 616–640. 10.1016/j.oceaneng.2021.10974110.1002/fld.3992.